

Article

Tetranuclear Copper Complexes with Bulky Aminoalcohol Ligands as Catalysts for Oxidative Phenoxazinone Synthase-like Coupling of Aminophenol: A Combined Experimental and Theoretical Study

Oksana V. Nesterova , Armando J. L. Pombeiro  and Dmytro S. Nesterov * 

Centro de Química Estrutural, Institute of Molecular Sciences, Instituto Superior Técnico, Universidade de Lisboa, 1049-001 Lisbon, Portugal

* Correspondence: dmytro.nesterov@tecnico.ulisboa.pt

Abstract: The new copper(II) complexes $[\text{Cu}_4(\text{pa})_4(\text{Bae})_4]\cdot\text{H}_2\text{O}$ (**1**) and $[\text{Cu}_4(\text{eba})_4(\text{Buae})_4]\cdot\text{H}_2\text{O}$ (**2**) (Hpa = propionic acid, HBae = 2-benzylaminoethanol, Heba = 2-ethylbutyric acid and HBuae = 2-butylaminoethanol) were synthesized by the interaction of a copper salt with a methanol solution of the respective ligands. The single-crystal X-ray diffraction analysis reveals that both compounds have a $\{\text{Cu}_4(\mu_3\text{-O})_4\}$ cubane-like core. Both compounds show pronounced phenoxazinone synthase-like activity towards the aerobic oxidation of *o*-aminophenol to phenoxazinone chromophore, with the maximum initial rates W_0 up to $3.5 \times 10^{-7} \text{ M s}^{-1}$, and exhibit complex non-linear W_0 vs. $[\text{catalyst}]_0$ dependences. DFT//CCSD theoretical calculations (B3LYP/ma-def2-TZVP//DLPNO-CCSD(T)/ma-def2-TZVPP) were employed to investigate the most challenging steps of catalyst-free and copper-catalysed *o*-aminophenol oxidation (formation of *o*-aminophenoxy radical). QTAIM analysis was used to study the key intermediates and weak interactions. Geometries and energies of intermediates and transition states were benchmarked against a series of popular DFT functionals. The results of the calculations demonstrate that a $\text{Cu}^{\text{II}}\text{-OO}\bullet$ copper-superoxo model catalyst decreases the calculated activation barrier from 28.7 to 19.9 kcal mol⁻¹ for the catalyst-free and copper-catalysed abstraction of the H atom from the hydroxyl group of *o*-aminophenol, respectively. Finally, both complexes **1** and **2** were studied as catalysts in the amidation of cyclohexane with benzamide to give *N*-cyclohexyl benzamide and *N*-methyl benzamide employing di-*tert*-butyl peroxide (DTBP) as the oxidant, with a conversion of 16%, and in the oxidation of cyclohexane to cyclohexanol with aq. H_2O_2 , with a conversion of 12%.



Citation: Nesterova, O.V.; Pombeiro, A.J.L.; Nesterov, D.S. Tetranuclear Copper Complexes with Bulky Aminoalcohol Ligands as Catalysts for Oxidative Phenoxazinone Synthase-like Coupling of Aminophenol: A Combined Experimental and Theoretical Study. *Catalysts* **2022**, *12*, 1408. <https://doi.org/10.3390/catal12111408>

Academic Editors: Victorio Cadierno and Raffaella Mancuso

Received: 28 September 2022

Accepted: 7 November 2022

Published: 10 November 2022

Publisher's Note: MDPI stays neutral with regard to jurisdictional claims in published maps and institutional affiliations.



Copyright: © 2022 by the authors. Licensee MDPI, Basel, Switzerland. This article is an open access article distributed under the terms and conditions of the Creative Commons Attribution (CC BY) license (<https://creativecommons.org/licenses/by/4.0/>).

Keywords: copper complexes; phenoxazinone synthase; aerobic *o*-aminophenol oxidation; reaction mechanisms; alkane functionalisation; DFT calculations; DLPNO-CCSD(T) calculations

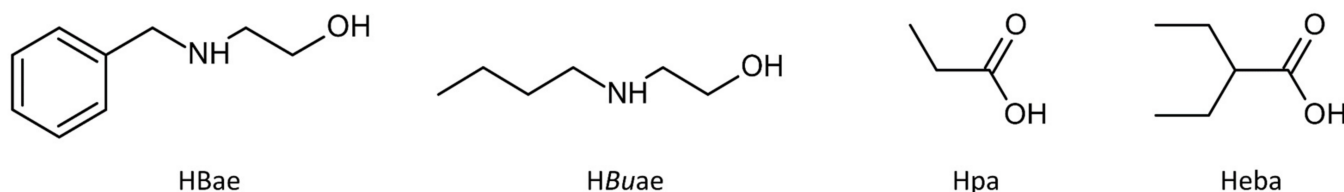
1. Introduction

The synthesis and investigation of homo- and heterometallic polynuclear complexes is an important field of contemporary chemistry. The presence of several metal centres at close proximity facilitates red-ox and spin coupling interactions that have a marked effect on catalytic [1–5] and magnetic properties [6–8]. Natural enzymes often contain polynuclear active centres, e.g., in methane monooxygenases (iron and copper dimers) [9], catechol oxidase (copper dimer) [10], photosystem II (Mn_4Ca) [11] and many others, for which the mechanistic investigations unambiguously indicate the participation of two or more metal centres in catalytic intermediates [12,13]. Thus, the synthesis of polynuclear complexes containing proper surroundings of metal centres can often be considered as a biomimetic approach towards novel catalytic systems.

Our synthetic strategy towards polynuclear coordination compounds is based on spontaneous self-assembly, where one of more metals is typically introduced in a zerovalent form [14–16]. Aerobic oxidation of this powdered metal induces deprotonation of

the hydroxyl groups of alcohol ligands, forcing their bridging coordination mode [14]. Another advantage of this technique is the absence (or reduced amount) of anions in the reaction mixture. Metal salts also can be used as starting materials in the spontaneous self-assembly approach. The presence of bulky aliphatic substituents in flexible chelating ligands is a second important feature of our strategy. Polynuclear complexes with a Schiff base and saturated N,O donor ligands could have pronounced catalytic activities [3,17]. However, their solubility in organic solvents is often limited, forming obstacles to the application of the respective complexes in homogeneous catalysis. The introduction of bulky hydrophobic groups not only sterically isolates and stabilises polynuclear species [18–20], but also makes them soluble in organic non-polar solvents, typically not adequate for complexes of this type [21,22]. Using this strategy, we described various homo- and heterometallic polynuclear complexes active in the sp^3 C–H hydroxylation [23–26] or amidation processes [21,22,24], and in the phenoxazinone synthase-like aerobic oxidation of aminophenols [27].

Oxidative coupling of the substituted *o*-aminophenol (OAPH) to phenoxazinone chromophore (PXCR) is a natural process, occurring during the biosynthesis of Actinomycin D [28–30], an antitumor drug that has application in medicine. This biological process is catalysed by the phenoxazinone synthase (PHS), which contains a polynuclear copper active centre [31,32]. The construction of efficient artificial catalytic systems [10], including those based on multicopper cores [33,34], became an important research direction. Recently, we described mono- and tetranuclear copper complexes with carboxylate and aminoalcohol ligands which showed unusual behaviour in the oxidation of OAPH [27]. In continuation of this research line, we now report the synthesis, characterisation and catalytic activity study of the two novel tetranuclear complexes $[Cu_4(pa)_4(Bae)_4] \cdot H_2O$ (1) and $[Cu_4(eba)_4(Buae)_4] \cdot H_2O$ (2) (Hpa = propionic acid, HBae = 2-benzylaminoethanol, Heba = 2-ethylbutyric acid and HBuae = 2-butylaminoethanol, Scheme 1). Both complexes act as efficient catalysts for the aerobic oxidation of OAPH to PXCR under ambient conditions. To gain further insights into the catalytic mechanisms, we conducted a theoretical DFT/ *ab initio* study of the principal steps of the metal-free aerobic oxidation of OAPH, as well as copper-catalysed reactions. Moreover, both complexes were studied as catalysts towards oxidative amidation and hydroxylation of cyclohexane.



Scheme 1. Structural formula of 2-benzylaminoethanol (HBae), 2-butylaminoethanol (HBuae), propionic acid (Hpa) and 2-ethylbutyric acid (Heba).

2. Results

2.1. Synthesis and Spectroscopic Analysis

Complexes **1** and **2** were synthesised using the self-assembly reaction of $Cu(NO_3)_2$ (**1**) or $Cu(BF_4)_2$ (**2**) with a methanol solution of aminoalcohol (2-benzylaminoethanol for **1** or 2-butylaminoethanol for **2**) and carboxylic acid (propionic for **1** or 2-ethylbutyric acid for **2**) in the presence of triethylamine, using the molar synthetic ratio of Cu:aminoalcohol:carboxylic acid = 1:3:1. The reactions were initiated and brought to completion by heating (50–60 °C) and stirring in open air. Dark-blue solutions were obtained at the end of both reactions. Dark-blue microcrystals of **1** suitable for the X-ray crystallographic study were formed after two months from the resulting solution without any additional procedures, while the crystals of **2** grew within two weeks.

The IR spectra of **1** and **2** show complex patterns in the 400–2000 cm^{-1} region (Figures S3 and S4) and confirm the presence of both carboxylate and aminoalcoholate

ligands. The weak broad bands in the 3400–3500 cm^{-1} region are attributed to the $\nu(\text{OH})$ frequencies of solvated water molecules. The very strong bands in the 1550–1600 cm^{-1} and 1390–1410 cm^{-1} regions are assigned to the antisymmetric and symmetric COO^- stretching frequencies of the carboxylate ligands, respectively.

2.2. Crystal Structures

The single-crystal X-ray analysis reveals that the tetranuclear complexes $[\text{Cu}_4(\text{pa})_4(\text{Bae})_4]\cdot\text{H}_2\text{O}$ (**1**) and $[\text{Cu}_4(\text{eba})_4(\text{Buae})_4]\cdot\text{H}_2\text{O}$ (**2**) have similar structural configurations based on the cubane-like molecular core $\{\text{Cu}_4(\mu_3\text{-O})_4\}$, where the copper atoms are linked together by $\mu_3\text{-O}$ bridges from aminoalcoholate ligands (Figure 1). The 2-benzylaminoethanolate (**1**) and 2-butylaminoethanolate (**2**) ligands are deprotonated forms of the corresponding alcohols and reveal bidentate bridging–chelate coordination, while deprotonated propionic (**1**) and 2-ethylbutyric (**2**) acids show a monodentate coordination mode.

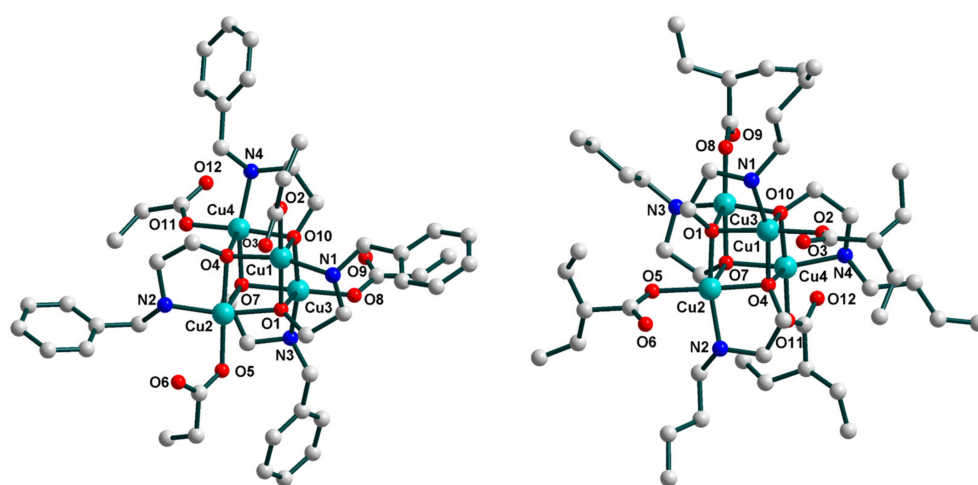


Figure 1. Ball-and-stick representations of the crystal structures of **1** (left) and **2** (right) with partial atom numbering schemes. H atoms are omitted for clarity. Colour scheme: Cu, cyan; O, red; N, blue; C, grey.

Both complexes contain four crystallographically independent copper(II) atoms, each of which is penta-coordinated and has distorted square-pyramidal geometry, with an O_4N donor set formed by donor atoms from carboxylate and aminoalcoholate ligands. The equatorial $\text{Cu}-\text{O}(\text{N})$ bond lengths in **1** and **2** vary from 1.905(5) to 2.0359(11) Å, and the apical $\text{Cu}-\text{O}$ bond distances are in the range 2.3386(8)–2.5784(9) Å (Table S2). The *cis* and *trans* $\text{O}-\text{Cu}-\text{O}(\text{N})$ bond angles span from 74.12(3) to 113.75(19)° and from 159.7(2) to 179.45(4)°, respectively. The non-bonded intermetallic $\text{Cu}\cdots\text{Cu}$ separations within the tetranuclear cores of **1** and **2** span in the range of 2.8843(3)–3.4592(3) and 2.9040(12)–3.4568(11) Å, respectively.

The tetranuclear molecules in **1** and **2** are joined together by strong hydrogen bonding of two types, $\text{O}-\text{H}\cdots\text{O}$ and $\text{N}-\text{H}\cdots\text{O}$, involving oxygen and nitrogen atoms from aminoalcohols, carboxylate ligands and uncoordinated water molecules as well [for **1**: $\text{N1}-\text{H1}\cdots\text{O12}^{\text{a}}$ ($a = x, 1.5 - y, 0.5 + z$), $\text{D}-\text{A} = 2.9895(14)$ Å, $\text{D}-\text{H}\cdots\text{A} = 152.5(17)^\circ$; $\text{N2}-\text{H2}\cdots\text{O9}^{\text{a}}$, $\text{D}-\text{A} = 3.0682(15)$ Å, $\text{D}-\text{H}\cdots\text{A} = 145.1(16)^\circ$; $\text{N3}^{\text{b}}-\text{H3}^{\text{b}}\cdots\text{O6}$ ($b = x, 1.5 - y, -0.5 + z$), $\text{D}-\text{A} = 2.8835(14)$ Å, $\text{D}-\text{H}\cdots\text{A} = 165.7(17)^\circ$; $\text{N4}^{\text{b}}-\text{H4}^{\text{b}}\cdots\text{O3}$, $\text{D}-\text{A} = 2.9859(14)$ Å, $\text{D}-\text{H}\cdots\text{A} = 144.9(17)^\circ$; $\text{O13}-\text{H6}\cdots\text{O9}^{\text{a}}$, $\text{D}-\text{A} = 2.8873(16)$ Å, $\text{D}-\text{H}\cdots\text{A} = 167(2)^\circ$; $\text{O13}-\text{H5}\cdots\text{O3}$, $\text{D}-\text{A} = 2.9399(16)$ Å, $\text{D}-\text{H}\cdots\text{A} = 172(3)^\circ$ and for **2**: $\text{N1}-\text{H1}\cdots\text{O9}^{\text{c}}$, $\text{D}-\text{A} = 2.989(8)$ Å, $\text{D}-\text{H}\cdots\text{A} = 146.9^\circ$; $\text{N2}-\text{H2}\cdots\text{O12}^{\text{c}}$ ($c = 0.5 - x, -0.5 + y, z$), $\text{D}-\text{A} = 3.031(8)$ Å, $\text{D}-\text{H}\cdots\text{A} = 146.7^\circ$; $\text{N3}^{\text{c}}-\text{H3}^{\text{c}}\cdots\text{O3}$, $\text{D}-\text{A} = 2.960(8)$ Å, $\text{D}-\text{H}\cdots\text{A} = 163.5^\circ$; $\text{N4}^{\text{c}}-\text{H4}^{\text{c}}\cdots\text{O6}$, $\text{D}-\text{A} = 2.997(8)$ Å, $\text{D}-\text{H}\cdots\text{A} = 151.6^\circ$; $\text{O13}-\text{H13D}\cdots\text{O3}$, $\text{D}-\text{A} = 3.049(13)$ Å, $\text{D}-\text{H}\cdots\text{A} = 156.3^\circ$; $\text{O13}-\text{H13C}\cdots\text{O12}^{\text{c}}$, $\text{D}-\text{A} = 2.974(14)$ Å, $\text{D}-\text{H}\cdots\text{A} = 137.3^\circ$]. As a result, similar 1D supramolecular chains of **1** and **2** are formed (Figure 2).

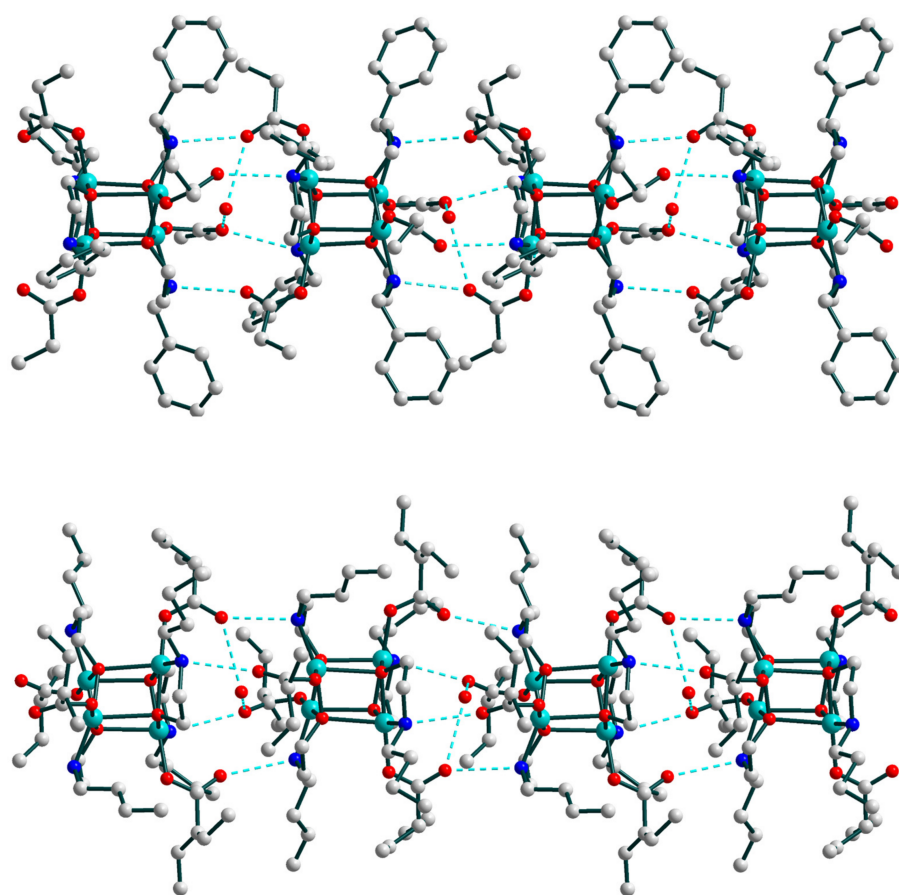


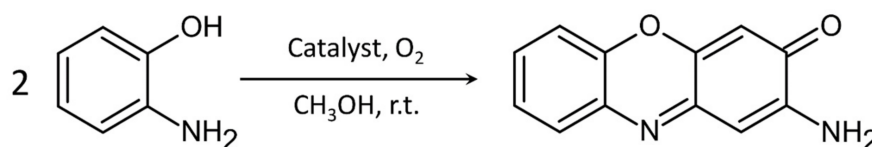
Figure 2. Fragments of the supramolecular chain in **1** (top) and **2** (bottom). H atoms are omitted for clarity. Colour scheme: Cu, cyan; O, red; N, blue; C, grey.

The observed H-bonding network results in a close packing of the neighbouring tetranuclear molecules. The intermetallic Cu...Cu non-bonded distances within the chains are in the range of 5.727–6.658 and 5.962–6.672 Å for **1** and **2**, respectively. The bulky substituents of the organic ligands present in both crystal structures are arranged in a way that prevents the formation of the supramolecular assemblies of higher than 1D dimensionality.

2.3. Catalytic Activity

2.3.1. Phenoxazinone Synthase-Like Activity

Both complexes **1** and **2** were studied as catalysts in the aerobic oxidation of *o*-aminophenol (OAPH) to phenoxazinone chromophore (PXCR) (Scheme 2).



Scheme 2. The model reaction for phenoxazinone synthase-like activity.

The addition of catalytic amounts of the catalyst to an OAPH solution in methanol affords a rapid growth of the absorption at 435 nm expected for PXCR [28]. The first test using 0.4 mM of **1** and 10 mM of OAPH revealed the initial reaction rate $W_0 = 7.0 \times 10^{-8} \text{ M s}^{-1}$. The respective UV spectra of the catalytic solutions are shown in Figure 3. The accumulations of PXCR are of linear character in the studied range. The blank test in the absence of a catalyst and using $[\text{OAPH}]_0 = 10 \text{ mM}$ shows two orders of lower activity, with $W_0 = 6 \times 10^{-10} \text{ M s}^{-1}$. This rate agrees with that previously reported ($9 \times 10^{-10} \text{ M s}^{-1}$) under similar conditions [27].

Complex **2** reveals an activity comparable to that of **1**, as evidenced by the initial rate of $7.5 \times 10^{-8} \text{ M s}^{-1}$ for $[2]_0 = 0.5 \text{ mM}$.

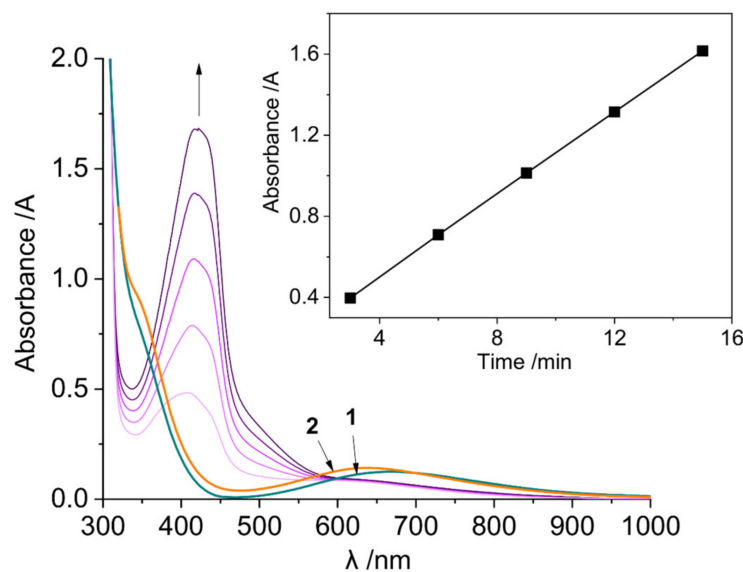


Figure 3. Increase in the band at 435 nm, attributable to the phenoxazinone chromophore (PCXR), over time in the aerobic oxidation of OAPH (10 mM) catalysed by **1** (0.4 mM) in methanol. Orange and green solid lines show the absorption spectra of **1** and **2** at the 0.4 mM concentration. The inset shows the evolution of the 435 nm absorption with time.

The W_0 vs. $[\text{cat}]_0$ dependence is shown in Figure 4. In general, both complexes show similar behaviour, where two distinct stages can be elucidated: an initial linear stage for $[\text{Cu}]_{\text{total}} < 1.5 \text{ mM}$ and an exponentially increasing stage for $[\text{Cu}]_{\text{total}} > 1.5 \text{ M}$ (hereafter the concentration of catalysts are given in terms of mols of all copper present in solution).

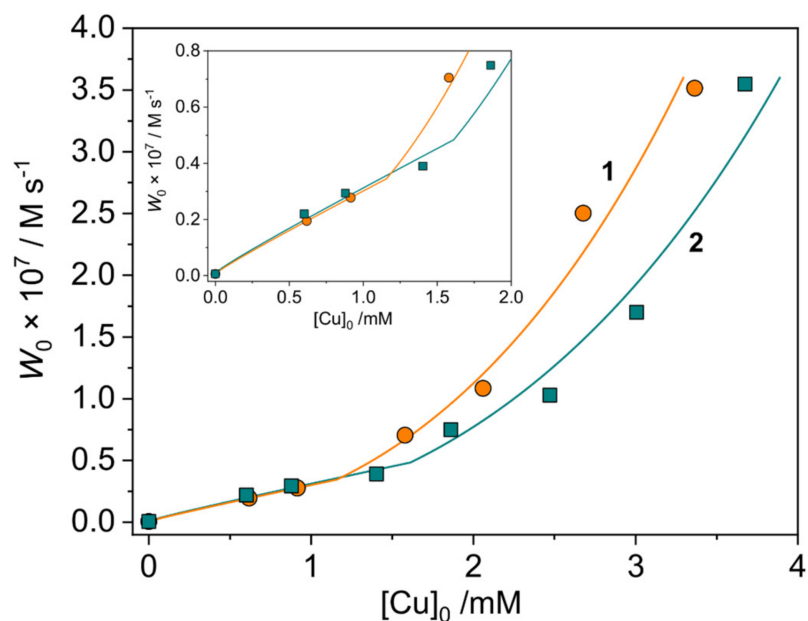


Figure 4. Dependences of the initial reaction rates W_0 on the initial concentrations of catalysts **1** and **2** (total copper concentrations $[\text{Cu}]_0$ are used) in the aerobic oxidation of OAPH (10 mM) in methanol at room temperature. Symbols are experimental data and solid lines are theoretical fits. Inset shows the low concentration range in detail.

In an attempt to interpret such a dependence, we applied the model described by us earlier [27], which presumes the existence of equilibrium between tetranuclear (Cu_4) and dinuclear (Cu_2) species, where the catalytic activity of Cu_2 is negligible compared to that of Cu_4 . Hence, the reaction equation $W_0 = k_{\text{eff}4}[\text{Cu}_4] + k_{\text{eff}2}[\text{Cu}_2]$ can be simplified to $W_0 = k_{\text{eff}4}[\text{Cu}_4]$, where k_{eff} are effective reaction constants that include all quasistationary components. Considering the equilibrium constant $K = [\text{Cu}_4]/[\text{Cu}_2]^2$ and the material balance $[\text{Cu}]_0 = 4[\text{Cu}_4] + 2[\text{Cu}_2]$, one can obtain the linear equation $\frac{[\text{Cu}]_0}{W_0^{1/2}} = aW_0^{1/2} + b$, where $[\text{Cu}]_0$ is the total initial concentration of copper, $a = \frac{4}{k_{\text{eff}4}}$ and $b = \frac{2}{(k_{\text{eff}4} K)^{1/2}}$. The representation of W_0 vs. $[\text{cat}]_0$ dependences in linearised coordinates is shown in the Figure 5.

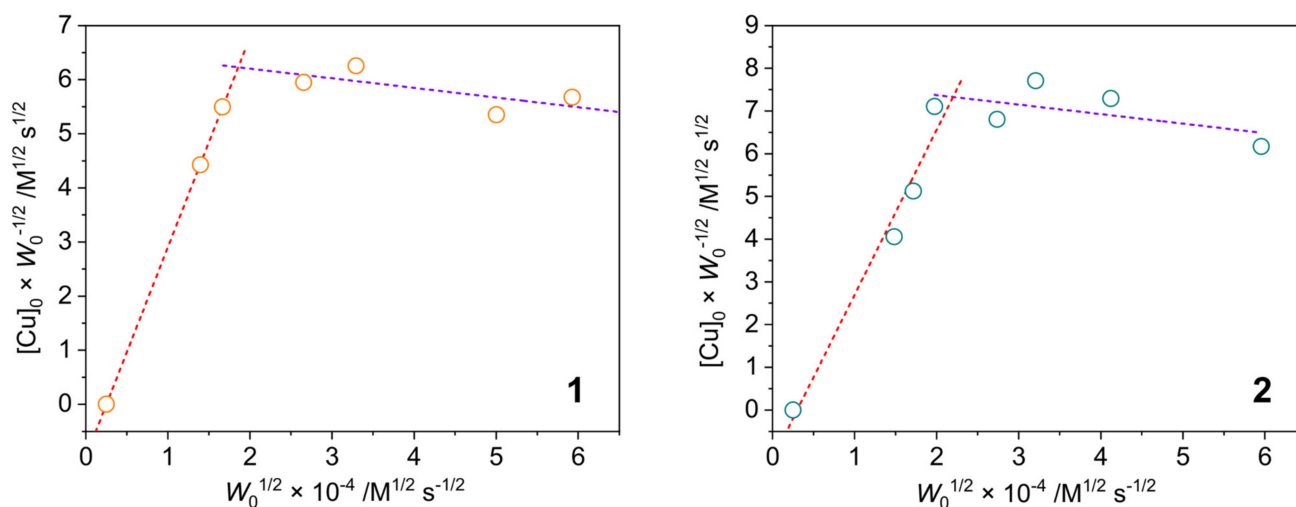


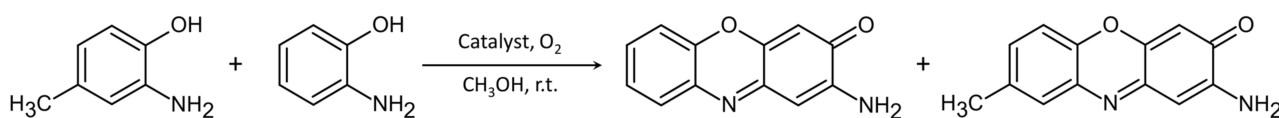
Figure 5. The raw data (Figure 4) plotted in $[\text{Cu}]_0/W_0^{1/2}$ vs. $W_0^{1/2}$ coordinates, showing the presence of two quasilinear phases in both curves. Symbols are experimental data and dotted lines are linear fits. Both quasilinear regions were used to generate the curves on the Figure 4 plots.

One can see that the whole data cannot be fitted as a single line, rather showing two linearised regions with the intersection points of $[\text{Cu}]_0 = 1.2$ and 1.6 mM for **1** and **2**, respectively. Moreover, the region with higher reaction rates reveals negative slopes of the lines for both **1** and **2**, suggesting that the condition $k_{\text{eff}4} \gg k_{\text{eff}2}$ is not satisfied and the model is not applicable in the present case. Another factor could be the interaction of the copper complexes with OAP, which could act as a chelating ligand and quench the activity of the complexes when the ratio $[\text{OAP}]_0/[\text{cat}]_0$ is high enough (low catalyst loading).

The reaction rates exhibited by catalysts **1** and **2** (W_0 up to $3.5 \times 10^{-7} \text{ M s}^{-1}$, corresponding to the $\text{TOF} = 1 \times 10^{-4} \text{ s}^{-1}$) can be considered as high, compared to the typical range of rates from 1×10^{-8} to $1 \times 10^{-6} \text{ M s}^{-1}$ [10]. The prominent activity of both complexes can be associated to their polynuclear nature, where the close proximity of metal centres promotes interaction between the catalytically active intermediates. A further increase in rates could be achieved through the design of compounds of higher nuclearity towards possible higher access of the polynuclear cage surface.

The oxidation of an equimolar mixture of *o*-aminophenol and 2-amino-*p*-cresol (10 mM each) catalysed by **1** (0.4 mM) resulted in both normal and methyl-substituted phenoxazinone chromophores in a 1:1 ratio (by GC analysis) after 60 min (Scheme 3). Such behaviour is expected for 2-amino-*p*-cresol, for which the formation of a phenoxazinone chromophore is not possible due to the presence of a methyl group. The evolution of the visible absorption with time is depicted in Figure S6. Using the extinction coefficient of the non-substituted chromophore ($2.4 \times 10^4 \text{ M}^{-1} \text{ cm}^{-1}$), the reaction rate of $1 \times 10^{-7} \text{ M s}^{-1}$ can be deduced. This value is slightly higher than that obtained for the oxidation of 10 mM of OAP only (Figure 3). This increase can be explained by the twice higher concentration of

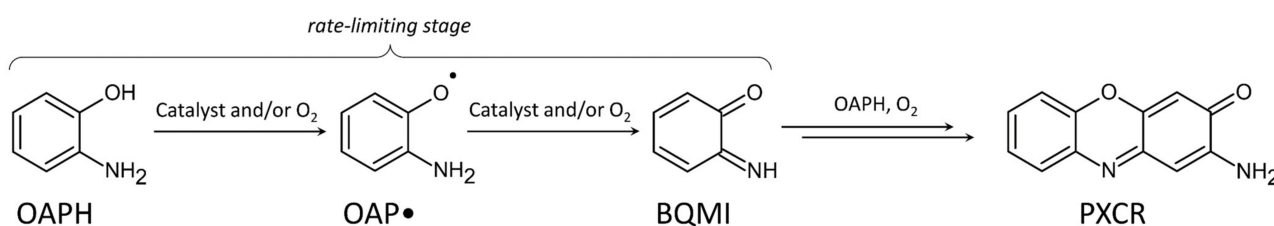
a substrate. In addition, the difference between extinction coefficients of the normal and methyl-substituted phenoxazinone chromophores was neglected.



Scheme 3. Aerobic oxidation of equimolar mixture of 2-amino-*p*-cresol and *o*-aminophenol (10 mM each) catalysed by **1** (0.4 mM), in methanol, affords normal and methyl-substituted phenoxazinone chromophores.

The TD-DFT analysis of the chromophores was performed at the PBE0/ma-def2-TZVPP level for the B3LYP/ma-def2-TZVP optimised geometries in methanol. The calculated UV/Vis spectra are depicted in Figure S7. The first excited state S1 involves mostly HOMO – 1 → LUMO and HOMO → LUMO transitions, all of the $\pi \rightarrow \pi^*$ type, and correspond to 454.7 and 454.4 nm for normal and methyl-substituted chromophores, respectively (Figure S8, Listings S1 and S2). These values are rather close to the one observed experimentally (435 nm). In contrast, the wavelengths of the S0 → S2 transitions are considerably different: 375.9 and 387.7 nm for normal and methyl-substituted chromophores, respectively. This effect can be explained by the contribution of the molecular orbitals of a methyl group to the S2 excited state (Figure S8, Listing S2). Therefore, even the presence of a small substituent may substantially change the absorption wavelengths and strengths.

The oxidative formation of *o*-aminophenoxy radical (OAP•) and *o*-iminobenzoquinone (BQMI) is known to be the rate-limiting step during the aerobic OAPH oxidation to phenoxazinone chromophore (Scheme 4) [10]. Although transition metal catalysts (e.g., those of copper) can serve as terminal oxidants in all oxidation steps [27,34,35], the principal role of a catalyst is commonly considered in the formation of the BQMI intermediate in the presence of O₂ [10]. Remarkably, despite many efforts that have been made to investigate this reaction mechanism experimentally, only limited data are available in terms of the theoretical description of possible reaction pathways of BQMI formation [36].



Scheme 4. The rate-limiting stage of the OAPH oxidation towards the PXCR formation.

While the enzymatic reaction starts with the two-electron oxidation of OAPH [29], artificial systems, as well as catalyst-free oxidations, are known to be sensitive to the radical traps or even initiated by stable radicals, such as 2,2,6,6-tetramethyl-1-piperidinyloxy (TEMPO) [37,38]. Therefore, the transformation of OAPH to BQMI may proceed through the OAP• radical. In our theoretical calculations, we considered the H atom abstraction from the hydroxyl group as a first step in the aerobic oxidation of OAPH. The interaction of OAPH with ³O₂ (reactant ³R₁) affords two stable intermediates, where the O₂ molecule is bonded either to hydroxyl group or amino group (Figures 6 and 7, Scheme 5). The close examination of non-covalent interaction reveals that both oxygen atoms of O₂ form weak attractive interactions with OAPH (Figure 6), namely N–H...O and C–O...O (for ³I_{1a}), and C–H...O and O–H...O (for ³I_{1b}).

The electron densities at the respective bond critical points for ³I_{1a} are nearly equal for N–H...O and C–O...O contacts ($\rho(r_{\text{BCP}}) = 3.7 \times 10^{-3}$ a.u.), which correspond to the binding energy of -0.08 kcal mol⁻¹ per contact, according to the model developed by Emamian

and Lu [40]. For the ${}^3I_{1b}$ configuration (Figures 6 and 7), the O–H...O and C–H...O contacts appear to be different in binding energies, as evidenced by the electron densities of 4.0×10^{-3} and 1.7×10^{-3} a.u., respectively. For these densities, the model [40] predicts the binding energies of -0.16 and 0.36 kcal mol $^{-1}$, respectively. From the DFT//CCSD calculations, we found the enthalpies of OAPH + 3O_2 interactions to be -0.68 and -0.28 kcal mol $^{-1}$ (for ${}^3I_{1a}$ and ${}^3I_{1b}$, respectively), thus showing that the abovementioned model can correctly predict the interaction magnitude but it is less relevant in certain cases [41], such as very weak interactions. It must be noted that the binding energy is based on the electronic energy only (with or without basis set counterpoise correction) [42], which does not include the zero point and vibrational energies.

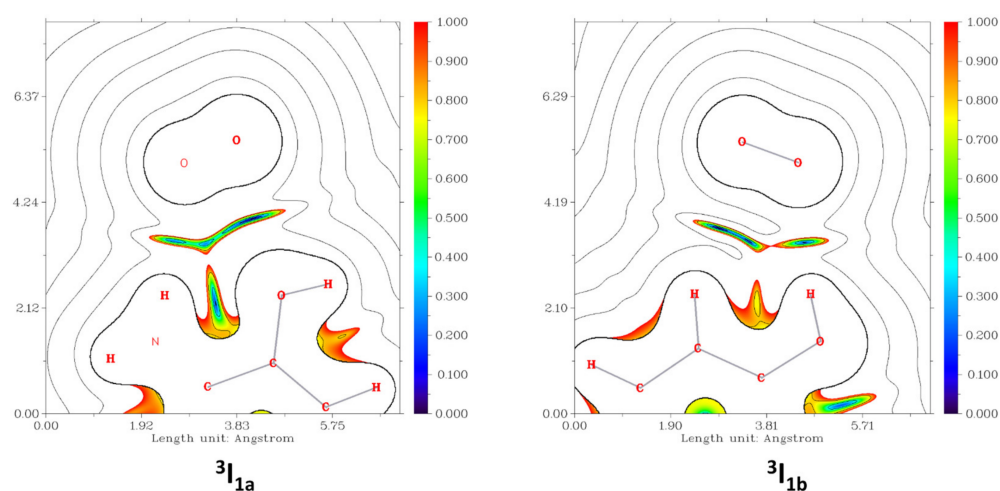


Figure 6. Reduced density gradient (RDG) [39] plot for the optimized (B3LYP/ma-def2-TZVP) intermediates ${}^3I_{1a}$ and ${}^3I_{1b}$ highlighting the weak non-covalent attractive interactions (blue regions) at the bond critical points between O atoms of the O_2 molecule and H or O atoms of the OAPH molecule. The absent N–X and O–O bonds in the left figure indicate that the respective bonds are slightly out of plane.

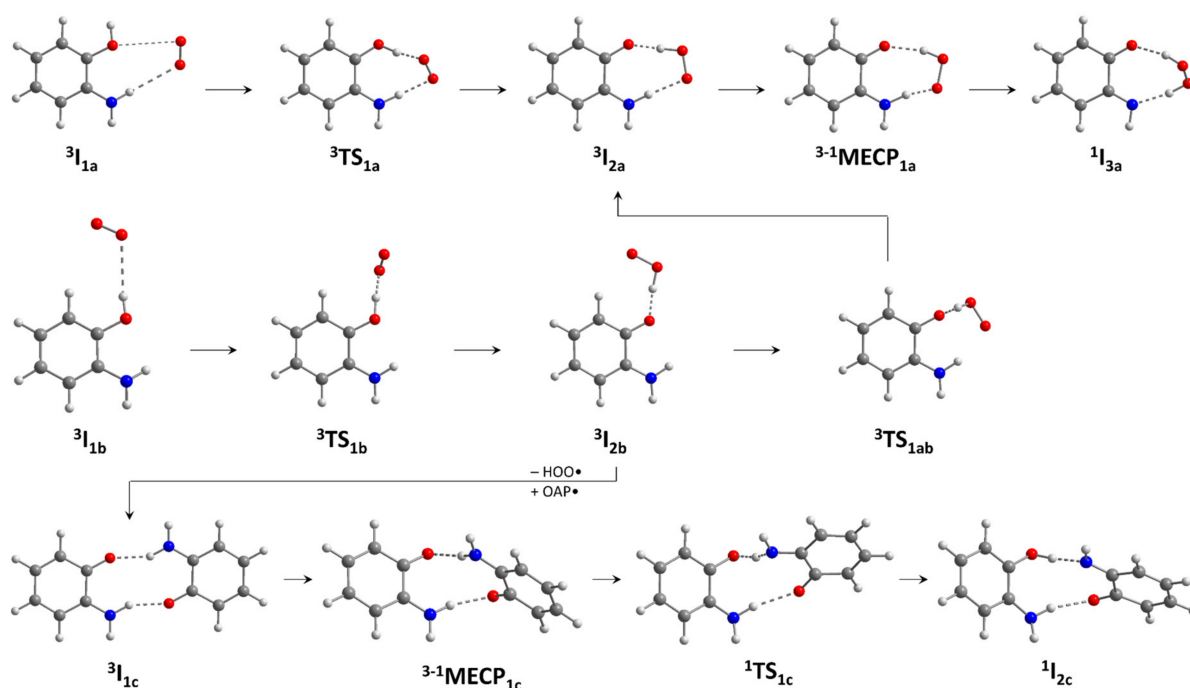
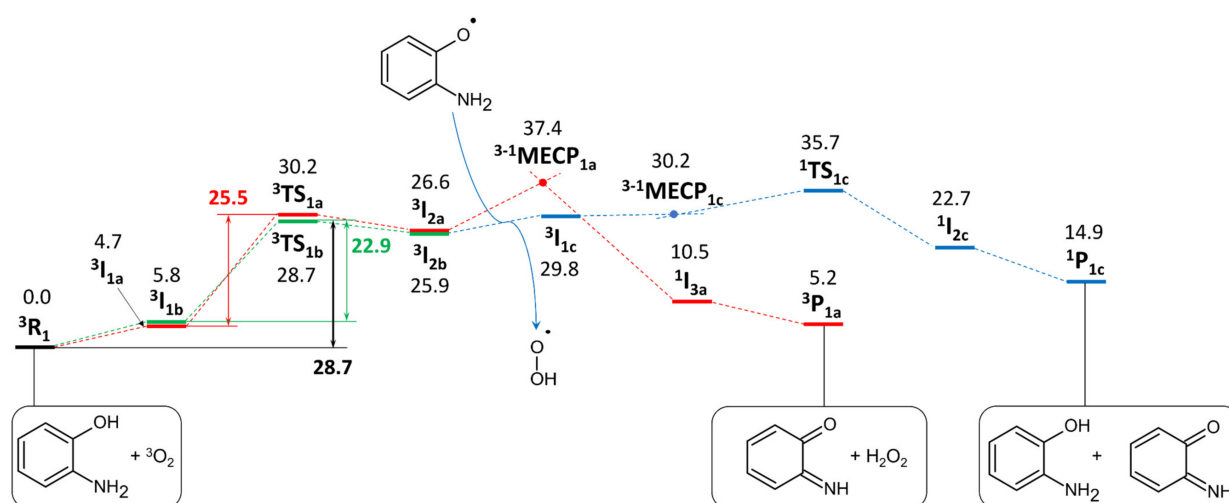


Figure 7. Calculated molecular geometries of intermediates and transition states for the catalyst-free aerobic oxidation of OAPH to BQMI.



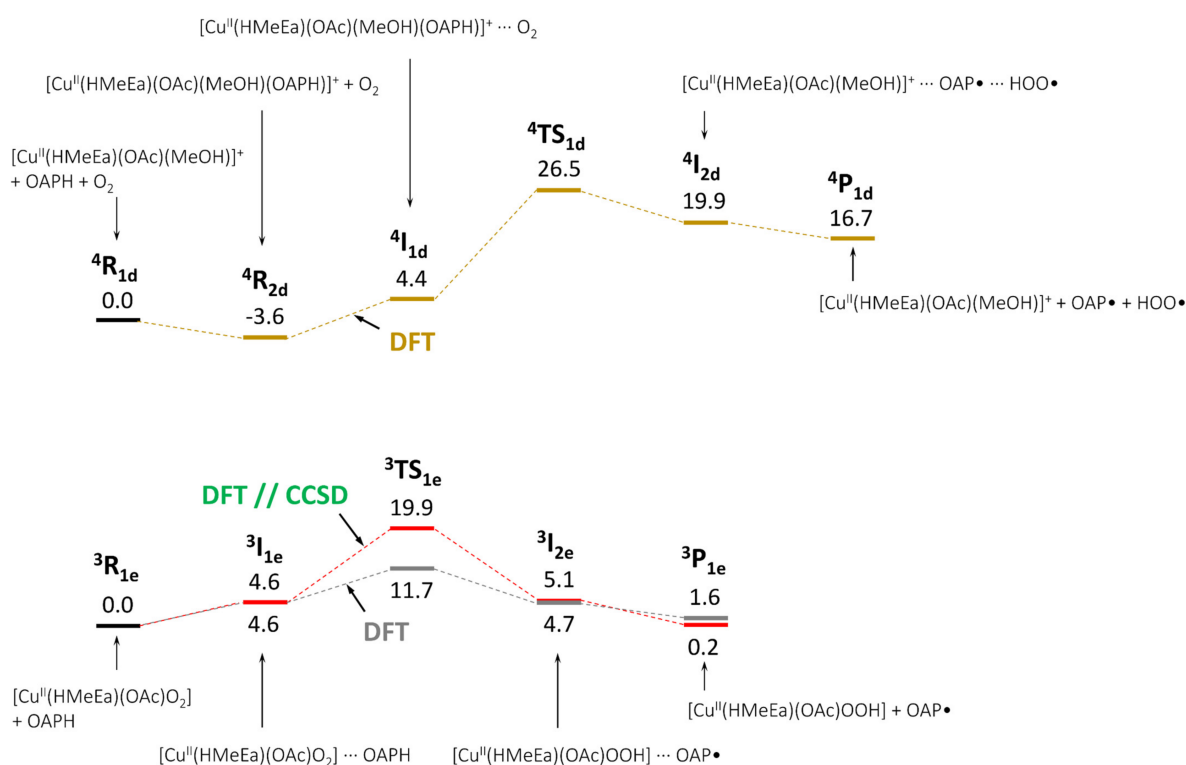
Scheme 5. Free energy profile for the aerobic oxidation of OAPH (R = reactant, I = intermediate, TS = transition state, P = product, MECP = minimum energy crossing point) calculated at the B3LYP/ma-def2-TZVP//DLPNO-CCSD(T)/ma-def2-TZVPP level. The numbers show the change of the free Gibbs energy, ΔG (kcal mol⁻¹), relative to the starting reactant 3R_1 . The combination of free OAP• with HOO•, which is a probable intermediate between ${}^3I_{2b}$ and ${}^3I_{1c}$, has practically equal energy to that for the ${}^3I_{2b}$ intermediate (-0.1 kcal mol⁻¹ relative to ${}^3I_{2b}$), thus the respective intermediate was omitted for clarity.

Both intermediates ${}^3I_{1a}$ and ${}^3I_{1b}$ underwent transformation to radical intermediates ${}^3I_{2a}$ and ${}^3I_{2b}$, respectively, through H transfer (Figure 7, Scheme 5). While the barriers are rather different, the resulting intermediates ${}^3I_{2a}$ and ${}^3I_{2b}$ have nearly equal Gibbs energy. The further fate of intermediates ${}^3I_{2a}$ and ${}^3I_{2b}$ depends on the behaviour of the •OOH radical. The configuration ${}^3I_{2a}$ can be further transformed to the BQMI–H₂O₂ intermediate ${}^1I_{3a}$ via the triplet–singlet minimum energy crossing point ${}^{3-1}MECP_{1a}$ with a barrier of only 10.8 kcal mol⁻¹ (Scheme 5). Due to the very close energies of the intermediates ${}^3I_{2a}$ and ${}^3I_{2b}$ and very low barrier of 1.5 kcal mol⁻¹ (transition state ${}^3TS_{1ab}$, Figure 7), the ${}^3I_{2b}$ intermediate can transform to ${}^3I_{2a}$ and vice versa. Another possibility is the elimination of the •OOH radical with subsequent disproportionation to form BQMI and OAPH (Figure 7, Scheme 5). The possibility of disproportionation was evidenced from the kinetic studies in some cobalt-catalysed systems [43,44]. However, this pathway appears to be less favourable due to the necessity of the presence of two reactive OAP• radicals, while the W_0 vs. [OAPH]₀ dependence of a catalyst-free oxidation does not show acceleration with the [OAPH]₀ growth (Figure S5) [45]. Furthermore, the overall Gibbs energy changes for both ${}^3R_1 \rightarrow {}^1P_{1a}$ and ${}^3R_1 \rightarrow {}^1P_{1c}$ are less favourable for the latter process.

According to the above data, the OAPH → OAP• reaction in methanol has the lowest barrier of 28.7 kcal mol⁻¹ for ${}^3TS_{1b}$ in methanol solution, which is slightly lower than the barrier between 3R_1 and ${}^3TS_{1a}$ of 30.2 kcal mol⁻¹ (Scheme 5). These barriers are not too high to impede the catalyst-free reaction completely, but account for its low rate, which agrees with the experimentally determined $W_0 = 6 \times 10^{-10}$ M s⁻¹ for [OAPH]₀ = 10 mM at ambient conditions. It should be noted that the barriers obtained from the pure DFT calculations were found to be different and often lower than for the DFT//CCSD ones. For instance, the Gibbs energy of the transition state ${}^3TS_{1a}$ undergoes an increase from 19.8 to 30.2 kcal mol⁻¹ after applying the CCSD correction (Scheme S1). The same tendency is found with the range-separated ω B97X-D4 [46,47] or double-hybrid B2PLYP [48] functionals applied in a certain case (Table S3). It was also found that the chosen DFT//CCSD methods afford the barrier ${}^3I_{1a} \rightarrow {}^3TS_{1a}$ very close (0.9 kcal mol⁻¹ difference) to that obtained from heavier and computationally more expensive calculations with denser integration grids, SMD solvation model at all stages and tighter SCF convergence criteria (Table S3).

Obviously, the reaction proceeds much faster in the case the catalyst decreases the activation energy. Since theoretical calculations of polynuclear complexes are computationally demanding, we considered a putative model of mononuclear copper species with aminoalcohol and carboxylate ligands, where OAPH and/or O₂ could coordinate to the copper centre. OAPH is a “classical” N,O donor ligand and known to form coordination compounds with various metals. Ghosh et al. suggested that the coordination of OAPH through the deprotonated oxido-group to a dinuclear zinc complex is most favourable [36]. However, a search via the Cambridge Structural Database (CCDC Inc., Cambridge, England; ver. 5.43; June 2022) [49] reveals that such a coordination is less frequent for coordination compounds: 3, 3 and 19 hits were found for O-, N- and O,N donor chelate bonding, respectively, for pure OAPH, and 4, 10 and 42 hits, respectively, including substituted OAPH ligands.

Firstly, we modelled the N donor coordination of the OAP molecule in the [Cu^{II}(HMeEa)(OAc)(MeOH)(OAPH)]⁺...O₂ complex (where HMeEa = N-methylethanolamine and HOAc = acetic acid; these ligands are related to those in complexes **1** and **2** but require fewer computational costs due to a smaller number of atoms and the absence of a flexible *n*-butyl group) that results in a stable intermediate ⁴I_{1d} (Figures S9 and S10). However, the relaxed scan (Figure S9) along the H...O distance (where O belongs to O₂ molecule) revealed that abstraction of the H atom from the hydroxyl group leads to the decooordination of the OAP• because its amino group becomes strictly planar and, in this way, sterically not able to coordinate a metal centre. Since this decooordination occurs at (or immediately after) the H transfer transition stage ⁴TS_{1d} (Figure S9), the activation energy for such a reaction is expected to be equal or higher than that for the metal-free ³I_{1b} → ³I_{2b} process. The DFT calculations resulted in a barrier of 30.1 kcal mol⁻¹ (Scheme 6), which is comparable to that for the metal-free reaction (Scheme 5).



Scheme 6. Free energy profiles of two reaction pathways for the aerobic oxidation of OAPH (R = reactant, I = intermediate, TS = transition state, P = product) catalysed by putative species [Cu(HMeEa)(OAc)], calculated at the B3LYP/ma-def2-TZVP (DFT) and B3LYP/ma-def2-TZVP//DLPNO-CCSD(T)/ma-def2-TZVPP (DFT//CCSD) levels. The numbers show the change of the free Gibbs energy, ΔG (kcal mol⁻¹), relative to the starting reactant R.

In the next approximation, the bidentate coordination of OAPH to the $[\text{Cu}^{\text{II}}(\text{HMeEa})(\text{OAc})]^+$ complex was considered, where the H atom in the HMeEa ligand is from the deprotonated hydroxyl group of OAPH (Figure S11). However, while the formation of the O-centred radical upon oxidation by Cu(II) is known to be possible [50], an attempt to model such a reaction did not afford a stable $\text{Cu}(\text{I})\cdots\text{OAP}\bullet$ intermediate (optimisation of the reaction product results in the reactant geometry, i.e., the $\text{OAP}\bullet$ radical readily couples with the Cu(I) centre).

In the next approach, we modelled putative copper–superperoxo species. Their formation is expected from the reaction $\text{M}^{n-1} + {}^3\text{O}_2 \rightarrow \text{M}^n\text{-OO}\bullet$, which constitutes a typical part of the metal-mediated aerobic oxidations [3,51–53]. The decrease in the absorption bands at 665 and 636 nm (for **1** and **2**, respectively; Figure 3), attributable to d-d transitions of Cu(II) cations in the catalytic solutions, agrees with the assumption that a part of copper exists in the Cu(I) state. The interaction of the OAPH molecule with the $[\text{Cu}^{\text{II}}(\text{HMeEa})(\text{OAc})\text{O}_2]$ complex results in the stable intermediate ${}^3\text{I}_{1e}$, where the OAPH molecule makes a broad interaction surface with the aminoalcohol ligand. The integration of a reduced density gradient (RDG) isosurface (Figure 8, left) reveals the participation of 0.0335 electrons in the H-bonded and van der Waals interactions between OAPH and $[\text{Cu}^{\text{II}}(\text{HMeEa})(\text{OAc})\text{O}_2]$. Apart from the $\text{O}\cdots\text{H}\cdots\text{O}$ hydrogen bond ($\rho(r_{\text{BCP}}) = 0.025$ a.u.), the strongest possible interaction is the $\text{N}\cdots\text{H}\cdots\text{C}$ one, as evidenced by the $\rho(r_{\text{BCP}})$ of 0.011 a.u. (Figure 8, right). The interaction enthalpy between OAPH and $[\text{Cu}^{\text{II}}(\text{HMeEa})(\text{OAc})\text{O}_2]$ was found to be -6.4 kcal mol $^{-1}$. The alternative intermediate ${}^3\text{I}_{1ea}$, where the OAP is bridged by the $\text{O}\cdots\text{H}\cdots\text{O}$ hydrogen bond only (Figure S12), has 1.8 kcal mol $^{-1}$ higher Gibbs energy than ${}^3\text{I}_{1e}$ (by the DFT) but proceeds to the intermediate ${}^3\text{I}_{2e}$ through the same transition state ${}^3\text{TS}_{1e}$.

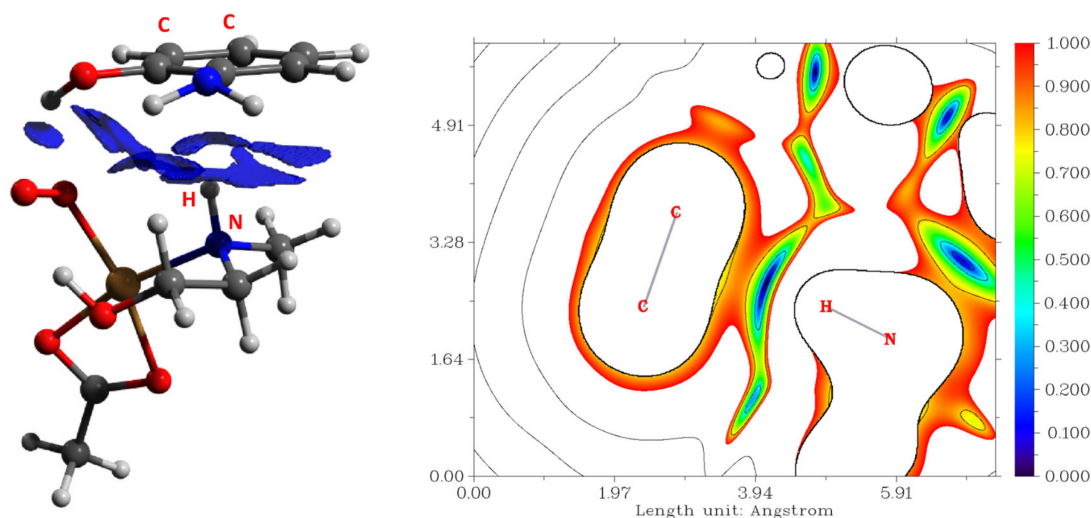


Figure 8. Left: optimised structure of the intermediate ${}^3\text{I}_{1e}$ showing the part of RDG isosurface (0.01 a.u. level) highlighting the non-covalent interactions between OAPH and copper catalyst. Right: the RDG plot showing the nature of non-covalent interactions for the strongest bonding between N–H group of the catalyst and C–C atoms of the OAPH (the respective atoms are labelled in the left figure).

The energy of the barrier ${}^3\text{TS}_{1e}$ of the H transfer reaction and formation of the $\text{OAP}\bullet$ radical is 19.9 kcal mol $^{-1}$ (Scheme 6). This value is substantially lower than the catalyst-free ${}^3\text{R}_1 \rightarrow {}^3\text{TS}_{1b}$ barriers of 28.7 and 30.2 kcal mol $^{-1}$ (Scheme 5). The analysis of the spin density discloses that most of the spin population (1.76) is localised on the copper and oxygen atoms of the Cu–OO \bullet superoxo fragment (Table S4), where the d_{yz} and d_{z^2} orbitals of the copper atom contribute (8.5, 7.4 and 7.4% for d_{yz} and 3.4, 4.8 and 3.7% for d_{z^2} , for ${}^3\text{I}_{1d}$, ${}^3\text{TS}_{1d}$ and ${}^3\text{I}_{2d}$, respectively) to one of the spin-up molecular orbitals. During the reaction, the spin density is transferred to the OAPH molecule (Figure 9), eventually leading to the H abstraction and release of the $\text{OAP}\bullet$ radical. The catalyst-free process exhibits a similar change of the spin density during the H transfer reaction (Figure 10, Table S5).

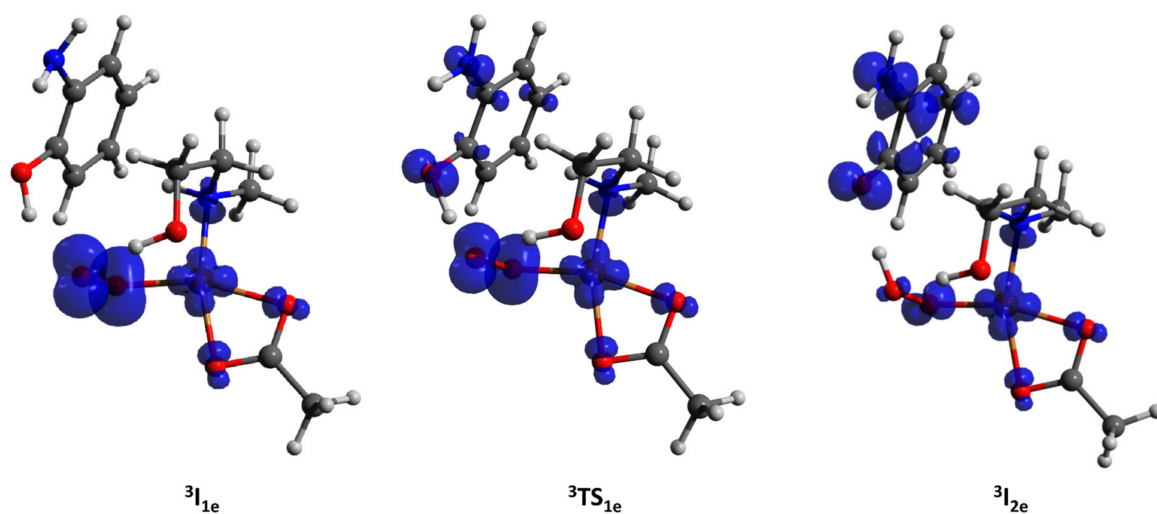


Figure 9. Isosurfaces of spin densities (0.01 a.u.) of the intermediates ${}^3I_{1e}$ and ${}^3I_{2e}$, and transition state ${}^3TS_{1e}$.

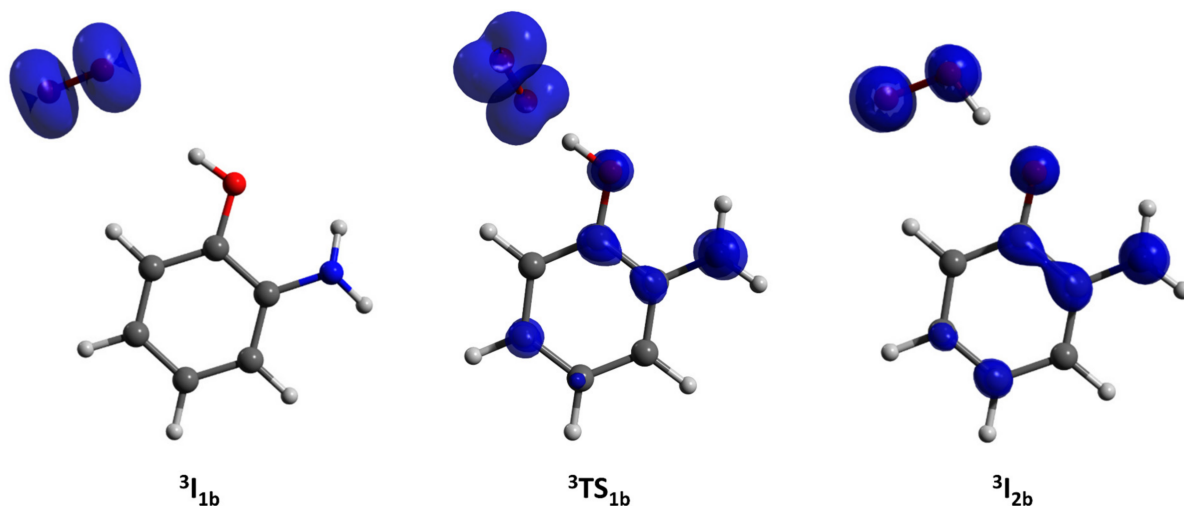


Figure 10. Isosurfaces of spin densities (0.01 a.u.) of the intermediates ${}^3I_{1b}$ and ${}^3I_{2b}$, and transition state ${}^3TS_{1b}$ (catalyst-free process).

The lower energy barrier for the copper-catalysed reaction can be explained by two reasons. First, the non-covalent interactions between the OAPH and copper catalyst (Figure 8) stabilise the resulting assembly, in this way increasing the probability of successful H atom transfer from the hydroxyl group to O_2 . Next, Löwdin atomic charges (Table S3) indicate a significant increase in electronegativity of the oxygen atom of O_2 abstracting hydrogen from the hydroxyl group, while the respective Löwdin spin population is twice higher for the metal-free starting configuration (Table S3). It is known that the coordination of O_2 to a metal centre increases its nucleophilicity [54], in this way facilitating attacks on the positively charged hydrogen atom.

A series of DFT functionals (ω B97X-D4 [46,47], M06-2X [55], TPSSh [56–58], B3LYP [59], PBE0 [60,61], M06-L [62], TPSS [56], PBE [63], BP86 [64,65], B97-3c [66]) was evaluated to determine the reliability of the transition state geometries using the ${}^3I_{1a} \rightarrow {}^3TS_{1a} \rightarrow {}^3I_{2a}$ reaction as an example. As can be seen, the functionals TPSSh, B3LYP, PBE0, M06-L, TPSS, PBE, BP86, B97-3c gave a similar disposition of the dioxygen molecule relative to the OAPH one (Figure S15), with the OAP $O \cdots H$ distances varying from 1.04 (PBE0) to 1.241 Å (PBE) and the $O \cdots H \cdots O$ angle ranging from 169.20 (PBE0) to 173.13° (B97-3c). The ω B97X-D4 and M06-2X functionals resulted in slightly different geometries, where the H atom is closer to the OAPH oxygen atom ($d(O \cdots H) = 0.979$ Å), at the same time showing comparable

separations (ranging from 1.880 to 2.022 Å) between the H atom and oxygen atoms from O₂ (Figure S15).

The Gibbs energies of the ³TS_{1a} and ³I_{2a} states relative to the ³I_{1a} one are listed in Table S6. As can be seen, pure GGA and meta-GGA functionals predict the ΔG energies of ³TS_{1a} and ³I_{2a} to be significantly lower than hybrid functionals. For the difference between intermediate structures ³I_{2a} and ³I_{1a}, whose geometries are less variable than that of the transition state, the lowest ΔG of 8.7 kcal mol⁻¹ was obtained by the BP86 functional, while the highest one of 18.5 kcal mol⁻¹ by the M06-2X functional. After the correction of electronic energies by single-point DLPNO-CCSD(T) calculations, all the final ΔG values become very close, ranging from 19.8 (M06-L) to 22.3 kcal mol⁻¹ (TPSSH). The smallest difference between pure DFT and CCSD-corrected energies is exhibited by the M06-2X functional, which shows 90% of the final DLPNO-CCSD(T) energy (Table S6).

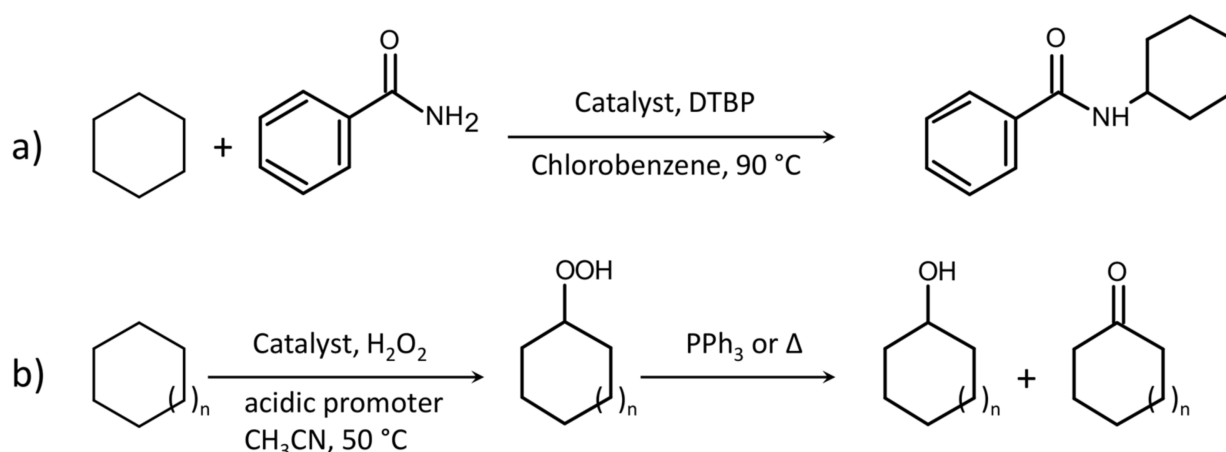
The Gibbs energies of the ³TS_{1a} transition state exhibit larger deviations. The lowest barrier of 6.8 kcal mol⁻¹ was predicted by the BP86 functional, while the highest barrier of 30.0 kcal mol⁻¹ by the ωB97X-D4 one. After applying the single-point DLPNO-CCSD(T) correction, the discrepancy becomes lower, but still not negligible (Table S6): the group of GGA and meta-GGA functionals shows Gibbs energies from 21.5 (M06-L) to 22.7 (TPSS) kcal mol⁻¹, while the hybrid functionals reveal higher energies from 24.5 (B3LYP) to 34.2 (ωB97X-D4) kcal mol⁻¹. The higher ΔG(³TS_{1a}) – ΔG(³I_{1a}) barriers observed for the case of ωB97X-D4 and M06-2X functionals can be associated to the respective geometries of the ³TS_{1a} transition states, which are slightly different from those obtained for other methods (Figure S15). However, all attempts to obtain the B3LYP-like geometry of ³TS_{1a} using the ωB97X-D4 and M06-2X functionals were unsuccessful.

The above results follow the known tendency of hybrid functionals to better estimate the electronic energy due to the inclusion of the Hartree–Fock exchange [67,68]. In the present case, the ΔG(³I_{2a}) – ΔG(³I_{1a}) Gibbs energies (after the DLPNO-CCSD(T) correction) were varied in the 2.5 kcal mol⁻¹ range, showing that all the functionals produce reliable geometries of the intermediates. A much larger spread in the case of ΔG(³TS_{1a}) – ΔG(³I_{1a}) energies (12.7 kcal mol⁻¹ after the DLPNO-CCSD(T) correction) indicates that the proper choice of a functional is crucial for the analysis of transition state geometries. The range-separated hybrid GGA ωB97X-D4 and hybrid meta-GGA M06-2X functionals are known to have high accuracy for weak non-covalent interactions [68–70]. Since the Gibbs energies produced by these two functionals are close to those obtained after the single-point DLPNO-CCSD(T) correction (Table S6), one may consider ωB97X-D4 and M06-2X functionals as a good choice for accurate energies. However, although the B3LYP functional underestimates the Gibbs energy barrier, the correction of an electronic energy by the coupled cluster method affords ΔG close to those exhibited by other hybrid functionals (Table S6). Considering that B3LYP performs faster than ωB97X-D4 and significantly faster than M06-2X functionals (Figure S16), the B3LYP functional, as a well-recognised calculation method, is an appropriate choice for the geometry optimisations of the transition states in the present case. The correction of the single-point energy obtained from higher-level calculations is necessary for the B3LYP calculations. These results completely agree with those suggested earlier for the B3LYP functional [71].

One should emphasise that the difference in the ³TS_{1a} geometries (Figure S15) and energies (Table S6) is stipulated by the great flexibility of the ³TS_{1a} structure, where the dioxygen molecule may occupy various positions. The reoptimisation of the more “rigid” transition state ³TS_{1e} by the M06-2X functional revealed the geometry to be very similar to that found using the B3LYP method (Figure S17).

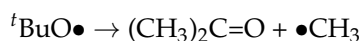
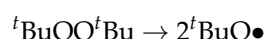
2.3.2. Amidation and Hydroxylation of Cyclohexane

Considering the prominent activity of **1** and **2** in the OAPH oxidation reaction, with the possible participation of radical intermediates, we studied the catalytic activity of both complexes in cyclohexane (CyH) functionalisation reactions, namely, peroxidative radical amidation and hydroxylation (Scheme 7).

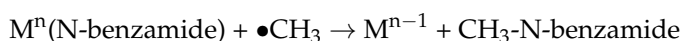
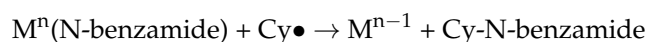
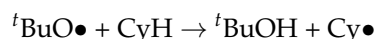


Scheme 7. The model reaction: amidation (a) and hydroxylation (b) of cyclohexane catalysed by complexes **1** and **2** ($n = 1$ or 3).

The reaction of 0.3 M of benzamide with 10 eq of CyH and 2 eq. of ^tBuOO^tBu in chlorobenzene in the presence of 1 mol% of the catalyst at 90 °C resulted in 16% conversion of benzamide after 24 h. The main products of the amidation reaction are N-cyclohexyl benzamide (Cy-N-benzamide) and N-methyl benzamide, with nearly equal amounts (Figure S18). The formation of the methyl derivative can be understood if one considers the large contribution of a β-scission [72] of the ^tBuO• radical, which becomes favourable at the reaction temperature (90 °C) and, possibly, in the presence of **1** or **2**:



where both ^tBuO• and •CH₃ radicals react with a copper–benzamide intermediate [22,24,73]:



The DFT//DLPNO-CCSD(T) calculations indicate that the metal-free β-scission reaction has a barrier of 12.9 kcal mol^{−1} and ΔG = −16.5 kcal mol^{−1} at 90 °C (383.15 K), in this way being a thermodynamically favourable process (Figure S19). The barrier increases to 13.1 kcal mol^{−1} and ΔG to −11.5 kcal mol^{−1} at the standard conditions (298.15 K, 25 °C). Both ^tBuO• and •CH₃ radicals readily abstract the H atom from CyH, with the subsequent trapping of the Cy• radical by the Cu(II)–benzamide intermediate, according to the expected reaction mechanism [73]. In a similar way, trapping the methyl radical by the Cu(II)–benzamide intermediate leads to N-methyl benzamide. The conversion level exhibited by **1** and **2** is comparable to that observed (20%) for the dinuclear copper complexes with N-butyldiethanolamine and N-*tert*-butyldiethanolamine [22], but is lower than the conversion found (55%) for piperazine-based Schiff-base copper complexes [22]. However, in the latter cases, the amounts of N-methyl benzamide were significantly lower, indicating that both **1** and **2** are efficient scavengers for methyl radicals.

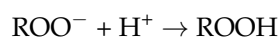
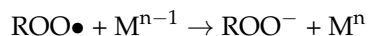
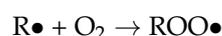
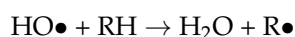
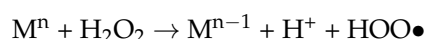
It is known that mono- and polynuclear complexes of copper are efficient catalysts for the oxidation of alkanes with peroxides [3]. Since complexes **1** and **2** contain N,O donor ligands that typically promote such a catalytic activity, we studied the catalytic properties of both compounds in the oxidation of cyclohexane with aqueous H₂O₂ in the presence of nitric acid promoter in acetonitrile. The reaction was initiated by adding five equivalents of H₂O₂ to CyH (0.2 M) in the presence of 2.5 mol% of nitric acid promoter and 0.1 mol% of the catalyst **1** or **2** (0.4 mol% if calculated per total copper amount). The

presence of small amounts of the acidic promoter typically has a promoting effect on the catalytic activity due to facilitation, e.g., of the proton transfer steps. Both complexes show similar initial reaction rates: $W_0 = 7.8 \times 10^{-7}$ and $1.1 \times 10^{-6} \text{ M s}^{-1}$ for **1** and **2**, respectively (Figure S20). The yield of products was 12% after 24 h, with an almost complete selectivity towards cyclohexanol, most likely due to the quantitative reduction in cyclohexyl hydroperoxide (main reaction product) to cyclohexanol by PPh_3 (see the Experimental section). These catalytic parameters are comparable to those exhibited by some systems reported earlier, e.g., by the heterometallic polynuclear Cu/Fe complex with *N-tert*-butyldiethanolamine ($W_0 = 3.9 \times 10^{-6} \text{ M s}^{-1}$ for 1.4 mol% of HNO_3 promoter), suggesting that both complexes **1** and **2** are promising catalysts for this type of reaction. It should be noted that activation of a strong sp^3 C–H bond of cyclohexane is a challenging process, where the yields demonstrated by most of the batch homo- or heterogeneous catalytic system do not exceed 35% [3].

The oxidation of cyclooctane under similar conditions resulted in a W_0 of 1.2×10^{-6} and $8.7 \times 10^{-7} \text{ M s}^{-1}$ for **1** and **2**, respectively (Figure S21), with an almost complete selectivity towards cyclooctanol. These reaction rates are close to those found for the oxidation of cyclohexane.

The high prevalence of alcohols in the course of the oxidation of cyclohexane and cyclooctane indicates the participation of the alkyl hydroperoxides (Scheme 7). Cyclohexyl hydroperoxide (CyOOH) was directly detected by the GC-MS technique (Figure S22), according to the analytical protocol earlier reported by some of us [21,24,74–78]. The chromatogram recorded before the addition of PPh_3 to the sample revealed that CyOOH is the main reaction product (Figure S22), since only traces of cyclohexanol and cyclohexanone were detected in this case. A similar test using cyclooctane as a substrate revealed the presence of several strong peaks on the chromatogram, completely disappearing after the addition of PPh_3 to the sample (Figure S23). The exact EI-MS spectrum of cyclooctyl hydroperoxide was not reported earlier. However, since both cyclohexyl and cycloheptyl hydroperoxides undergo elimination of H_2O and O_2H fragments upon ionisation, forming distinct $M-18$ and $M-33$ m/z peaks [79], one can expect similar behaviour for cyclooctyl hydroperoxide. The search towards the respective signals (Figure S24) revealed that the mass spectra of peaks I and II (Figure S25) can be interpreted as cyclooctyl hydroperoxide. A much stronger intensity of the 111 m/z peak than 126 m/z in the mass spectrum of II (Figure S25), expected for cycloalkyl hydroperoxides [79], allows its assignment to cyclooctyl hydroperoxide. The oxidation of cyclohexane and cyclooctane catalysed by complex **2** revealed the same chromatographic patterns of the products.

The oxidation of methylcyclohexane under similar conditions revealed the $1^\circ:2^\circ:3^\circ$ bond selectivities of 1:2:7 and 1:7:18 for **1** and **2**, respectively (Figure S26). Both selectivities are in the range expected for catalytic systems abstracting H atoms through the attack of a hydroxyl radical [80]. Considering this, as well as the presence of alkyl hydroperoxides as the main reaction products, the principal reaction pathway can be assigned to the broad class of mechanisms where the role of the catalyst concerns the generation of hydroxyl radicals upon reaction with H_2O_2 [3]:



3. Conclusions

We have synthesised the novel complexes $[\text{Cu}_4(\text{pa})_4(\text{Bae})_4]\cdot\text{H}_2\text{O}$ (**1**) and $[\text{Cu}_4(\text{eba})_4(\text{Buae})_4]\cdot\text{H}_2\text{O}$ (**2**), starting from copper salts and flexible aminoalcohol and carboxylic acids as pro-ligands, following the spontaneous self-assembly strategy. Single-crystal X-ray analyses revealed tetranuclear cores in both **1** and **2**. The Cu_4O_4 cores are surrounded by the bulky aliphatic and aromatic groups of the ligands, making the complexes soluble in aprotic hydrophobic solvents. Complexes **1** and **2** show a notable catalytic activity in the oxidative amidation of cyclohexane with benzamide, with the conversion of benzamide at 16%. The main reaction products are N-cyclohexyl and N-methyl benzamide. The formation of methylated benzamide can be understood in terms of β -scission of ${}^t\text{BuOO}{}^t\text{Bu}$ with the generation of a free methyl radical, which is a thermodynamically favourable process, according to the DFT//DLPNO-CCSD(T) calculations. Both **1** and **2** are active catalysts towards the oxidation of cyclohexane with aqueous H_2O_2 , showing reaction rates up to $1.1 \times 10^{-6} \text{ M s}^{-1}$ and yields of cyclohexanol of 12%.

The catalytic features of **1** and **2** were investigated in the aerobic oxidation of *o*-aminophenol (OAPH) to phenoxazinone chromophore (PXCR). Both complexes reveal a high catalytic activity, with a maximum initial reaction rate of $3.5 \times 10^{-7} \text{ M s}^{-1}$. The dependence of the initial reaction rate on the catalyst concentration was studied, showing that, for both catalysts **1** and **2**, it is linear up to 0.25 mM, beyond which a pronounced non-linear growth of the reaction rate is observed. A possible explanation could be the equilibria between the tetranuclear and smaller species in solution, where all species are catalytically active.

By using the combined DFT//DLPNO-CCSD(T) theoretical calculations, we also investigated the catalyst-free and copper-mediated formation of OAP• radicals and *o*-iminobenzoquinone (BQMI) upon the reaction of OAPH with O_2 , which is known to be the rate-limiting stage towards the formation of the phenoxazinone chromophore. Our results indicate that the highest barrier for the catalyst-free process is $28.7 \text{ kcal mol}^{-1}$ (according to DFT//DLPNO-CCSD(T)) and $19.8 \text{ kcal mol}^{-1}$ (according to DFT). Within the models studied, the lowest barrier for the copper-catalysed process was found to be $19.9 \text{ kcal mol}^{-1}$ (DFT//DLPNO-CCSD(T)) for the configuration where OAPH attacks a $\text{Cu}^{\text{II}}\text{-OO}\bullet$ peroxy species. The copper catalytic effect was associated not only to the coordination of OAPH, but also to the stabilisation of the starting intermediate through broad, non-covalent interactions between OAPH and the copper-peroxy catalyst.

We expect that the experimental and theoretical results of this study should help in the design of novel biomimetic catalytic systems and contribute to a better understanding of the mechanisms of OAPH oxidation, a reaction of biological relevance. Complexes of copper are versatile catalysts that promote a wide range of organic transformations [81–85]. Considering that complexes **1** and **2** were found to be active catalysts in three different types of reactions, one may expect that they may have a pronounced activity in other reactions, such as aerobic oxidations of $\text{sp}^3 \text{ C-H}$ bonds, cross-coupling or click chemistry, which deserve further investigation.

4. Experimental Section

4.1. General

All chemicals were of reagent grade and used as received. All experiments were carried out in air. Elemental analyses for C, H and N were carried out by the Microanalytical Service of the Instituto Superior Técnico. Infrared spectra ($4000\text{--}400 \text{ cm}^{-1}$) were recorded using an Agilent Cary 630 ATFT-IR (Agilent Technologies Inc., Santa Clara, CA, USA) spectrometer. UV/Vis spectra were recorded using a Perkin-Elmer Lambda 35 (PerkinElmer Inc., Waltham, MA, USA) spectrometer in the $330\text{--}600 \text{ nm}$ spectral range.

4.1.1. Synthesis of $[\text{Cu}_4(\text{pa})_4(\text{Bae})_4]\cdot\text{H}_2\text{O}$ (**1**)

$\text{Cu}(\text{NO}_3)_2\cdot 3\text{H}_2\text{O}$ (0.48 g, 2 mmol), 2-benzylaminoethanol (0.85 mL, 6 mmol) and triethylamine (0.7 mL, 2 mmol) were dissolved in CH_3OH (30 mL), forming a blue–green

solution which was magnetically stirred at 50–60 °C (30 min). Then, propionic acid (0.15 mL, 2 mmol) was added to this solution and the mixture was stirred for 1 h. Dark-blue microcrystals suitable for X-ray analysis were obtained after two months from the resulting dark-blue solution. Yield: 0.17 g, 29%. Anal. calc. for $C_{48}H_{70}Cu_4N_4O_{13}$ ($M = 1165.24$): C, 49.48; N, 4.81; H, 6.06%. Found: C, 49.48; N, 4.86; H, 6.11%.

4.1.2. Synthesis of $[Cu_4(eba)_4(Buae)_4] \cdot H_2O$ (**2**)

The preparation of complex **2** was like that of **1** but using $Cu(BF_4)_2 \cdot 2H_2O$ (0.55 g, 2 mmol), 2-butylaminoethanol (0.79 mL, 6 mmol) and 2-ethylbutyric acid (0.25 mL, 2 mmol), instead of copper nitrate, 2-benzylaminoethanol and propionic acid. Dark-blue microcrystals suitable for X-ray study were formed after two weeks from the resulting dark-blue solution. Yield: 0.16 g, 27%. Anal. calc. for $C_{48}H_{102}Cu_4N_4O_{13}$ ($M = 1197.49$): C, 48.14; N, 4.68; H, 8.59%. Found: C, 48.16; N, 4.56; H, 8.76%.

4.2. Crystallography

Details of the data collection and processing, structure solution and refinement are summarised in Table S1. The single-crystal X-ray data were acquired on a Bruker D8 Quest (for **1**) or AXS KAPPA APEX II (for **2**) diffractometer (Bruker AXS Inc., Madison, WI, USA). Cell parameters were retrieved and refined using the Bruker SAINT programme. SADABS was used for correction of absorption [86]. Both structures were solved by direct methods by means of SHELXT-2014/5 (for **1**) or Olex.Solve 1.5 (for **2**) and refined against F^2 using the SHELX-2018/3 (for **1**) or 2019/2 (for **2**) programme [87] (Table S1). The Olex2 1.5 (OlexSys Ltd., Durham, England) programme was used during the structures' refinement [88]. The hydrogen atoms of water molecules and N–H groups in **1** were localised and refined freely. The coordinates of the hydrogen atoms of the water molecule O13 in **2** were refined freely, while U_{iso} was fixed to $1.5U_{eq}$ of the O13 atom. The remaining H atoms in **1** and **2** were placed at calculated positions and refined using the riding model with $U_{iso} = 1.5U_{eq}$ (for methyl groups) or $U_{iso} = 1.2U_{eq}$ (for other groups). The ethyl groups C9–C12 of 2-ethylbutyric acid in **2** were found to be disordered over two sites with occupancies of 0.316(19) and 0.684(19). The geometries of the bulky *n*-butyl (C3–C6 and C15–C18) and ethyl (C8–C12, C20–C24, C32–C36 and C44–C48) groups were not satisfactory due to the large thermal motion. The respective C–C distances and C–C angles were restrained to ideal values obtained from the Cambridge Structural Database (CCDC Inc., Cambridge, England) [49] statistics. Anisotropic refinement of the atoms C3–C6 and C8–C12 was not successful, thus the isotropic refinement was used instead. The above issues originate from the weak high-angle diffraction data for **2**, for which $I/\sigma(I)$ is below 3 for $2\theta > 43^\circ$ (Figures S1 and S2).

Crystallographic data for the structures can be obtained free of charge from the Cambridge Crystallographic Data Centre via www.ccdc.cam.ac.uk/data_request/cif, quoting the deposition numbers CCDC 2201716 (**1**) and 2201715 (**2**).

4.3. Phenoxazinone Synthase Activity Study

The phenoxazinone synthase activity of **1** and **2** was monitored spectroscopically by recording the UV/Vis spectra in the 330–600 nm region (unless stated otherwise) at certain periods of time. Typically, 5 mL of a methanol solution of the complex of desired concentration (calculated as a full concentration of copper cations) was added to a 10 mL flask containing 5 mL of a methanol solution of *o*-aminophenol (OAPH). After 10 s of vigorous stirring a portion of the resulting mixture was transferred into a quartz cuvette (10 mm; Labbox (Labbox Labware S.L., Barcelona, Spain) MISQ-010-002) of the spectrophotometer, without further stirring. The extinction coefficient of $2.4 \times 10^4 \text{ M}^{-1} \text{ cm}^{-1}$ [27,34] was used to convert absorption to molar concentration.

4.4. Catalytic Amidation of Cyclohexane

The reactions were typically carried out under N_2 atmosphere in a thermostated Schlenk tube under vigorous stirring. Firstly, 6 mg (5 μmol) of the catalyst and 60.6 mg (0.5 mmol)

benzamide were introduced into the tube in the solid form. Then, chlorobenzene (1 mL) and cyclohexane (0.54 mL, 5 mmol) were added in this order. The oxidant (184 μ L, 1 mmol) t BuOO t Bu was then added at room temperature and the mixture was immediately frozen with liquid nitrogen; the gas atmosphere was pumped and filled with N₂ a few times to remove air. The frozen mixture was left to warm up under vacuum (to degasify) until it became liquid, and the above procedure was repeated. Finally, the Schlenk tube was filled with N₂ and the reaction mixture was heated at 90 °C for 24 h, with the possibility for gas to escape to compensate for the excessive pressure. The reaction mixtures were cooled to room temperature, 10 mL of CH₃CN and 1 mL of the solution of nitromethane (GC internal standard; 1 mL of CH₃NO₂ mixed with 9 mL of CH₃CN) were added and the resulting mixture was directly analysed by GC/GC-MS techniques.

4.5. Catalytic Hydroxylation of Cyclohexane

1.2 mg (1 μ mol) of the catalyst was added into a thermostated reaction vessel. Then, 4.1 mL of acetonitrile, 45 μ L (25 μ mol) of nitric acid solution (0.4 mL of HNO₃ 65% aq. mixed with 10 mL of acetonitrile), 0.5 mL of nitromethane solution (GC internal standard; 1 mL of CH₃NO₂ mixed with 9 mL of acetonitrile), 108 μ L (1 mmol) of cyclohexane and 0.28 mL (5 mmol) of H₂O₂ (50% aqueous) were added, in this order, at 50 °C under stirring (**Caution:** the combination of a hydrogen peroxide with organic compounds at elevated temperatures may be explosive!). The total reaction volume was 5 mL. Aliquots (ca. 0.5 mL) of the reaction mixture were transferred, upon cooling, into a vial containing an excess (ca. 150 mg) of solid Ph₃P (according to the method developed by Shul'pin [89]) and then analysed directly by gas chromatography GC/GC-MS techniques.

4.6. Gas Chromatography

A PerkinElmer Clarus 500 (PerkinElmer Inc., Waltham, MA, USA) gas chromatograph (BP-20 capillary GC column (SGE Inc., Trajan, Melbourne, Australia) 30 m \times 0.22 mm \times 25 μ m dimensions) equipped with an FID detector and a PerkinElmer Clarus 600 (PerkinElmer Inc., Waltham, MA, USA) gas chromatograph (two Zebron ZB-5 capillary GC columns (Phenomenex Inc., Torrance, CA, USA), 30 m \times 0.25 mm \times 25 μ m dimensions) equipped with an FID detector and with a PerkinElmer Clarus 600 C (PerkinElmer Inc., Waltham, MA, USA) electron impact mass spectrometer were used for quantitative and qualitative analyses of the catalytic mixtures (helium carrier gas was used). All Electron Ionisation (EI) mass spectra were recorded using 70 eV ionisation energy. The identification of product peaks at the chromatograms was made on the basis of the NIST v. 2.2 mass spectral database (PerkinElmer TurboMass v. 5.4.2.1617 software was used).

4.7. Theoretical Calculations

The ORCA 5.0.3 (Max-Planck-Institut für Kohlenforschung, Mülheim a. d. Ruhr, Germany) software package was used for all calculations [90–92]. Unless stated otherwise, the calculations were performed using B3LYP functional [59,93] with the minimally augmented ma-def2-SVP and ma-def2-TZVP basis sets [94] for non-metal and metal atoms, respectively (preliminary optimisation of intermediates and transition state geometries) or the ma-def2-TZVP basis set for all atoms (final calculations). Dispersion correction was introduced through the *D4* keyword (Grimme's atom-pairwise approach) [95]. The CCSD calculations were performed through the DLPNO-CCSD(T) scheme [96] using the ma-def2-TZVPP basis set [94] and *TightPNO* keyword. The iterative full LMP2 was disabled for the close-shell DLPNO-CCSD(T) calculations (keyword "*UseFullLMP2Guess False*"). The *AutoAux* keyword [97] was used to generate auxiliary basis sets in all cases. SCF convergence criteria corresponding to those invoked by the *TightSCF* keyword were automatically applied during geometry optimisations. Unless stated otherwise, the final enthalpies and Gibbs energies were obtained from the DFT calculations of geometry and vibrational energies where electronic energies were obtained from the CCSD calculations. Transition states were found using either nudged elastic band (NEB) [98] or relaxed scan methods, and refined at

the DFT level with DLPNO-CCSD(T) correction for electronic energy. The correctness of the transition state optimisation was confirmed by the presence of a single imaginary frequency. The minimum energy crossing points (MECPs) [99] for intersection of triplet and singlet surfaces were located using the *SurfCrossOpt* keyword. The solvent (methanol) effects were accounted for by means of the conductor-like polarisable continuum model (C-PCM) [100] for the DFT geometry optimisation and frequency calculations, and the solvation model based on density (SMD) [101] for the CCSD single-point calculations used to extract the exact electronic energy. The correction ΔG term of $1.89 \text{ kcal mol}^{-1}$ was added to the final Gibbs energies of single molecules to convert 1 atm to 1 M standard states [101]. The time-dependent DFT calculations (TD-DFT) were performed at the PBE0/ma-def2-TZVPP level using the Tamm–Dancoff approximation (TDA) [102]. The PBE0 hybrid functional is known to reproduce singlet excited states of organic molecules with sufficient accuracy [103,104]. The visualisation of spin density and reduced density gradient 3D isosurfaces was made using the Avogadro 1.2 (University of Pittsburgh, Pittsburgh, PA, USA) programme [105]. Analysis of bond critical points and non-covalent interactions indexes [39] was done using the Multiwfn 3.8 (University of Science and Technology, Beijing, People’s Republic of China) programme [106]. Cartesian coordinates of the DFT optimised structures are given in the Listings S3–S7.

Supplementary Materials: The following supporting information can be downloaded at: <https://www.mdpi.com/article/10.3390/catal12111408/s1>, Figure S1: Reflection intensity statistics ($I/\sigma(I)$ vs. 2θ) for **1**. Figure S2: Reflection intensity statistics ($I/\sigma(I)$ vs. 2θ) for **1**. Figure S3: IR spectrum of **1**. Figure S4: IR spectrum of **2**. Figure S5: Left: dependence of the initial reaction rate W_0 on the OAPH concentration in the catalyst-free aerobic oxidation of OAPH in methanol at room temperature. Right: change of the UV/Vis spectra for $[\text{OAPH}]_0 = 7.4 \times 10^{-4} \text{ M}$. The inset shows increase in the band at 435 nm. Figure S6: Increase in the band at 435 nm, attributable to the phenoxazinone chromophore (PCXR), over time in the aerobic oxidation of the mixture of *o*-aminophenol (OAPH, 10 mM) and 2-amino-*p*-cresol (10 mM) catalysed by **1** (0.4 mM) in methanol. Figure S7: Fragment of the TD-DFT calculated absorption spectra of the normal and methyl-substituted phenoxazinone chromophores. The absorptions corresponding to the first two strongest excitation states S1 and S2 are shown. Figure S8: Frontier molecular orbitals of the normal and methyl-substituted phenoxazinone chromophores (PBE0/ma-def2-TZVPP TD-DFT calculation using B3LYP/ma-def2-TZVP geometry in methanol; only singlet excitations were considered). Figure S9: Relaxed energy scan along the transition-state coordinate for the H atom abstraction from OAPH catalysed by the $[\text{Cu}^{\text{II}}(\text{HMeEa})(\text{OAc})(\text{MeOH})]^+$ complex. The final point at the 1.031 Å corresponds to the optimised geometry of the reaction product ${}^4\text{I}_{2\text{d}}$, while the respective separation in the reactant ${}^4\text{I}_{1\text{d}}$ configuration constitutes 3.046 Å. The figure shows the transition state ${}^4\text{TS}_{1\text{d}}$. Figure S10: Isosurfaces of the spin density (0.01 a.u. level) for the optimised intermediates ${}^4\text{I}_{1\text{d}}$ and ${}^4\text{I}_{2\text{d}}$ and transition state ${}^4\text{TS}_{1\text{d}}$. Figure S11: DFT-optimised structure of the $[\text{Cu}^{\text{II}}(\text{HMeEa})(\text{OAc})(\text{OAP})]$ complex, where OAP ligand is in the deprotonated state. Figure S12: DFT-optimised structure of the ${}^3\text{I}_{\text{ea}}$ intermediate. Figure S13: DFT-optimised structure of the ${}^3\text{I}_{1\text{e}}$ intermediate with partial numbering scheme. Figure S14: DFT-optimised structure of the ${}^3\text{I}_{1\text{b}}$ intermediate with partial numbering scheme. Figure S15: Molecular geometries and selected interatomic distances (Å) for the ${}^3\text{TS}_{1\text{a}}$ transition state optimised using different functionals. In all cases, the new transition states were found through the complete NEB-TS search between ${}^3\text{I}_{1\text{a}}$ and ${}^3\text{I}_{2\text{a}}$ intermediates using the respective functionals. Figure S16: Calculation timings for single-point and vibrational frequency calculations of the ${}^3\text{I}_{1\text{a}}$ intermediate using different DFT functionals. All geometries were preliminary optimised using the respective functionals. Figure S17: Molecular geometries and selected interatomic distances (Å) for the ${}^3\text{TS}_{1\text{e}}$ transition state optimised using B3LYP and M06-2X functionals. Figure S18: Fragments of the chromatograms showing the main reaction products (as well as benzamide) in the course of oxidative cyclohexane (2.9 M) oxidation with benzamide (0.3 M) in the presence of di-*tert*-butyl peroxide, DTBP (0.6 M) in chlorobenzene, catalysed by complexes **1** (top) and **2** (bottom) (29 mM). Figure S19: Comparison of free energy profiles for the β -scission of ${}^t\text{BuO}\bullet$ radical calculated at the B3LYP/ma-def2-TZVP (DFT) and B3LYP/ma-def2-TZVP//DLPNO-CCSD(T)/ma-def2-TZVPP (CCSD) levels at 90 °C (383.15 K) in chlorobenzene (SMD solvation model was used for all calculations). The numbers show the change of the free Gibbs energy, ΔG (kcal mol $^{-1}$), relative to the starting reactant ${}^2\text{R}_{1\text{f}}$. Figure S20: Accumulations of products (sum of cyclohexanol

and cyclohexanone) in the course of cyclohexane (0.2 M) oxidation with H_2O_2 (1 M) in the presence of nitric acid promoter (5 mM), catalysed by **1** (left) or **2** (right) (0.2 mM) in acetonitrile at 50 °C. Figure S21: Accumulations of cyclooctanol in the course of cyclooctane (0.2 M) oxidation with H_2O_2 (1 M) in the presence of nitric acid promoter (5 mM), catalysed by **1** or **2** (0.2 mM) in acetonitrile at 50 °C. Figure S22: Fragments of the chromatograms (Phenomenex ZB-5 column) showing the main reaction products before (bottom) and after (top) addition of PPh_3 in the course of cyclohexane (0.2 M) oxidation with H_2O_2 (1 M) in the presence of nitric acid promoter (5 mM), catalysed by **1** (0.2 mM) in acetonitrile at 50 °C after 60 min. Figure S23: Fragments of the chromatograms (Phenomenex ZB-5 column) showing the main reaction products before (bottom) and after (top) addition of PPh_3 in the course of cyclooctane (0.2 M) oxidation with H_2O_2 (1 M) in the presence of nitric acid promoter (5 mM), catalysed by **1** (0.2 mM) in acetonitrile at 50 °C after 60 min. Figure S24: Fragments of the chromatograms (Phenomenex ZB-5 column; top: 111 m/z signal, centre: 126 m/z signal, bottom: total chromatogram) showing the main reaction products before addition of PPh_3 in the course of cyclooctane (0.2 M) oxidation with H_2O_2 (1 M) in the presence of nitric acid promoter (5 mM), catalysed by **1** (0.2 mM) in acetonitrile at 50 °C after 60 min. Figure S25: EI-MS spectra of peaks I–IV (top down) depicted in Figures S23 and S24. Figure S26: Fragments of the chromatograms (SGE BP-20 column) showing the main reaction products after addition of PPh_3 in the course of methylcyclohexane (0.2 M) oxidation with H_2O_2 (1 M) in the presence of nitric acid promoter (5 mM), catalysed by **1** (0.2 mM) in acetonitrile at 50 °C. Scheme S1: Comparison of free energy profiles for the aerobic oxidation of OAPH (R = reactant, I = intermediate, TS = transition state, P = product, MECP = minimum energy crossing point) calculated at the B3LYP/ma-def2-TZVP (DFT) and B3LYP/ma-def2-TZVP//DLPNO-CCSD(T)/ma-def2-TZVPP (DFT//CCSD) levels. The numbers show the change of the free Gibbs energy, ΔG (kcal mol⁻¹), relative to the starting reactant ${}^3\text{R}_1$. Table S1: Crystal data and structure refinement for **1** and **2**. Table S2: Selected geometrical parameters (distances/Å and angles/°) for **1** and **2**. Table S3: Comparison of the barriers between ${}^3\text{TS}_{1a}$ and ${}^3\text{I}_{1a}$ states calculated at different theory levels. Table S4: Löwdin spin population and atomic charges for selected atoms in ${}^3\text{I}_{1e}$. Table S5: Löwdin spin population and atomic charges for selected atoms in ${}^3\text{I}_{1b}$. Table S6: Gibbs energies of ${}^3\text{TS}_{1a}$ and ${}^3\text{I}_{2a}$ states relative to ${}^3\text{I}_{1a}$ obtained using indicated DFT functionals before or after correction of electronic energies at the DLPNO-CCSD(T) level. Listing S1: Fragment of the ORCA output for the TD-DFT calculation of the phenoxazinone chromophore. Listing S2: Fragment of the ORCA output for the TD-DFT calculation of the methyl-substituted phenoxazinone chromophore. Listing S3: Cartesian coordinates of the intermediates and transition states optimised at the B3LYP-D4/ma-def2-TZVP level in methanol (C-PCM model). Listing S4: Cartesian coordinates of the ${}^3\text{I}_{1a}$ intermediate optimised using different functionals, ma-def2-TZVP basis set and tight integration grids in methanol (C-PCM model). Listing S5: Cartesian coordinates of the ${}^3\text{TS}_{1a}$ transition state optimised using different functionals, ma-def2-TZVP basis set and tight integration grids in methanol (C-PCM model). Listing S6: Cartesian coordinates of the ${}^3\text{I}_{2a}$ intermediate optimised using different functionals, ma-def2-TZVP basis set and tight integration grids in methanol (C-PCM model). Listing S7: Cartesian coordinates of the ${}^3\text{TS}_{1e}$ transition state optimised using M06-2X functional, ma-def2-TZVP basis set and tight integration grids in methanol (C-PCM model).

Author Contributions: Conceptualization, methodology, and investigation, O.V.N. and D.S.N.; catalytic investigation, O.V.N.; X-ray analysis and theoretical calculations, D.S.N.; writing—original draft preparation, O.V.N. and D.S.N.; methodology, resources, funding acquisition, writing—review and editing, A.J.L.P. All authors have read and agreed to the published version of the manuscript.

Funding: This work was supported by the Foundation for Science and Technology (FCT), Portugal (projects UIDB/00100/2020, UIDP/00100/2020 and LA/P/0056/2020 of Centro de Química Estrutural, contracts IST-ID/086/2018 and IST-ID/117/2018).

Data Availability Statement: Crystallographic data for the structures can be obtained free of charge from the Cambridge Crystallographic Data Centre via www.ccdc.cam.ac.uk/data_request/cif, quoting the deposition numbers CCDC 2201716 (**1**) and 2201715 (**2**).

Conflicts of Interest: The authors declare no conflict of interest.

References

1. Singh, D.; Buratto, W.R.; Torres, J.F.; Murray, L.J. Activation of Dinitrogen by Polynuclear Metal Complexes. *Chem. Rev.* **2020**, *120*, 5517–5581. [[CrossRef](#)] [[PubMed](#)]
2. Tang, J.; Zhao, L. Polynuclear organometallic clusters: Synthesis, structure, and reactivity studies. *Chem. Commun.* **2020**, *56*, 1915–1925. [[CrossRef](#)] [[PubMed](#)]
3. Nesterov, D.S.; Nesterova, O.V.; Pombeiro, A.J.L. Homo- and heterometallic polynuclear transition metal catalysts for alkane C-H bonds oxidative functionalization: Recent advances. *Coord. Chem. Rev.* **2018**, *355*, 199–222. [[CrossRef](#)]
4. Fang, J.; Zhang, B.; Yao, Q.F.; Yang, Y.; Xie, J.P.; Yan, N. Recent advances in the synthesis and catalytic applications of ligand-protected, atomically precise metal nanoclusters. *Coord. Chem. Rev.* **2016**, *322*, 1–29. [[CrossRef](#)]
5. Buchwalter, P.; Rose, J.; Braunstein, P. Multimetallic Catalysis Based on Heterometallic Complexes and Clusters. *Chem. Rev.* **2015**, *115*, 28–126. [[CrossRef](#)]
6. Vaz, M.G.F.; Andruh, M. Molecule-based magnetic materials constructed from paramagnetic organic ligands and two different metal ions. *Coord. Chem. Rev.* **2021**, *427*, 213611. [[CrossRef](#)]
7. Aguila, D.; Roubeau, O.; Aromi, G. Designed polynuclear lanthanide complexes for quantum information processing. *Dalton Trans.* **2021**, *50*, 12045–12057. [[CrossRef](#)]
8. Sharples, J.W.; Collison, D. The coordination chemistry and magnetism of some 3d-4f and 4f amino-polyalcohol compounds. *Coord. Chem. Rev.* **2014**, *260*, 1–20. [[CrossRef](#)]
9. Wang, V.C.C.; Maji, S.; Chen, P.R.Y.; Lee, H.K.; Yu, S.S.F.; Chan, S.I. Alkane Oxidation: Methane Monooxygenases, Related Enzymes, and Their Biomimetics. *Chem. Rev.* **2017**, *117*, 8574–8621. [[CrossRef](#)]
10. Dey, S.K.; Mukherjee, A. Catechol oxidase and phenoxazinone synthase: Biomimetic functional models and mechanistic studies. *Coord. Chem. Rev.* **2016**, *310*, 80–115. [[CrossRef](#)]
11. Yano, J.; Yachandra, V. Mn₄Ca Cluster in Photosynthesis: Where and How Water is Oxidized to Dioxygen. *Chem. Rev.* **2014**, *114*, 4175–4205. [[CrossRef](#)]
12. Nesterova, O.V.; Nesterov, D.S. Polynuclear Cobalt Complexes as Catalysts for Light-Driven Water Oxidation: A Review of Recent Advances. *Catalysts* **2018**, *8*, 602. [[CrossRef](#)]
13. Blomberg, M.R.A.; Borowski, T.; Himo, F.; Liao, R.Z.; Siegbahn, P.E.M. Quantum Chemical Studies of Mechanisms for Metalloenzymes. *Chem. Rev.* **2014**, *114*, 3601–3658. [[CrossRef](#)]
14. Nesterov, D.S.; Nesterova, O.V.; Kokozay, V.N.; Pombeiro, A.J.L. Polynuclear Heterometallic Complexes from Metal Powders: The “Direct Synthesis” Approach. *Eur. J. Inorg. Chem.* **2014**, *2014*, 4496–4517. [[CrossRef](#)]
15. Nesterov, D.S.; Graiff, C.; Tiripicchio, A.; Pombeiro, A.J.L. Direct synthesis and crystal structure of a new pentanuclear heterotrimetallic Cu/Co/Ni complex with 2-(dimethylamino)ethanol. Discussion of possible “butterfly-like” molecular structure types. *CrystEngComm* **2011**, *13*, 5348–5353. [[CrossRef](#)]
16. Nesterov, D.S.; Makhankova, V.G.; Kokozay, V.N.; Skelton, B.W. Direct synthesis and crystal structures of new heteropolynuclear complexes containing aminoalcohol ligands: From heterobi- (Co/Zn) to heterotrimetallic (Cu/Co/Zn) compounds. *Inorg. Chim. Acta* **2005**, *358*, 4519–4526. [[CrossRef](#)]
17. Liu, X.; Manzur, C.; Novoa, N.; Celedon, S.; Carrillo, D.; Hamon, J.-R. Multidentate unsymmetrically-substituted Schiff bases and their metal complexes: Synthesis, functional materials properties, and applications to catalysis. *Coord. Chem. Rev.* **2018**, *357*, 144–172. [[CrossRef](#)]
18. Nesterov, D.S.; Jezierska, J.; Nesterova, O.V.; Pombeiro, A.J.L.; Ozarowski, A. An unprecedented octanuclear copper core with C_{3i} symmetry and a paramagnetic ground state. *Chem. Commun.* **2014**, *50*, 3431–3434. [[CrossRef](#)]
19. Conceição, N.R.; Nesterova, O.V.; Rajnak, C.; Boca, R.; Pombeiro, A.J.L.; Guedes da Silva, M.F.C.; Nesterov, D.S. New members of the polynuclear manganese family: Mn^{II}₂Mn^{III}₂ single-molecule magnets and Mn^{II}₃M^{III}₈ antiferromagnetic complexes. Synthesis and magnetostructural correlations. *Dalton Trans.* **2020**, *49*, 13970–13985. [[CrossRef](#)]
20. Nesterov, D.S.; Alegria, E.C.B.A.; Jezierska, J. A new member of Cu^{II}₈ family: Synthesis, structure and magnetic properties of an octanuclear copper complex with N-tert-butyl-diethanolamine. *Inorg. Chim. Acta* **2017**, *460*, 83–88. [[CrossRef](#)]
21. Nesterova, O.V.; Nesterov, D.S.; Vranovicova, B.; Boca, R.; Pombeiro, A.J.L. Heterometallic Cu^{II}Fe^{III} and Cu^{II}Mn^{III} alkoxobridged complexes revealing a rare hexanuclear M₆(μ-X)₇(μ₃-X)₂ molecular core. *Dalton Trans.* **2018**, *47*, 10941–10952. [[CrossRef](#)] [[PubMed](#)]
22. Nesterova, O.V.; Nesterov, D.S.; Jezierska, J.; Pombeiro, A.J.L.; Ozarowski, A. Copper(II) Complexes with Bulky N-Substituted Diethanolamines: High-Field Electron Paramagnetic Resonance, Magnetic, and Catalytic Studies in Oxidative Cyclohexane Amidation. *Inorg. Chem.* **2018**, *57*, 12384–12397. [[CrossRef](#)] [[PubMed](#)]
23. Nesterova, O.V.; Kuznetsov, M.L.; Pombeiro, A.J.L.; Shul’pin, G.B.; Nesterov, D.S. Homogeneous oxidation of C-H bonds with m-CPBA catalysed by a Co/Fe system: Mechanistic insights from the point of view of the oxidant. *Catal. Sci. Technol.* **2022**, *12*, 282–299. [[CrossRef](#)]
24. Nesterova, O.V.; Pombeiro, A.J.L.; Nesterov, D.S. Novel H-Bonded Synthons in Copper Supramolecular Frameworks with Aminoethylpiperazine-Based Ligands. Synthesis, Structure and Catalytic Activity. *Materials* **2020**, *13*, 5435. [[CrossRef](#)] [[PubMed](#)]
25. Nesterova, O.V.; Kasyanova, K.V.; Makhankova, V.G.; Kokozay, V.N.; Vassilyeva, O.Y.; Skelton, B.W.; Nesterov, D.S.; Pombeiro, A.J.L. Stereospecific sp³ C-H oxidation with m-CPBA: A Co^{III} Schiff base complex as pre-catalyst vs. its Co^{III}Cd^{II} heterometallic derivative. *Appl. Catal. A* **2018**, *560*, 171–184. [[CrossRef](#)]

26. Nesterov, D.S.; Chygorin, E.N.; Kokozay, V.N.; Bon, V.V.; Boca, R.; Kozlov, Y.N.; Shul'pina, L.S.; Jezierska, J.; Ozarowski, A.; Pombeiro, A.J.L.; et al. Heterometallic Co^{III}₄Fe^{III}₂ Schiff Base Complex: Structure, Electron Paramagnetic Resonance, and Alkane Oxidation Catalytic Activity. *Inorg. Chem.* **2012**, *51*, 9110–9122. [[CrossRef](#)]
27. Nesterova, O.V.; Bondarenko, O.E.; Pombeiro, A.J.L.; Nesterov, D.S. Phenoxazinone synthase-like catalytic activity of novel mono- and tetranuclear copper(II) complexes with 2-benzylaminoethanol. *Dalton Trans.* **2020**, *49*, 4710–4724. [[CrossRef](#)]
28. Freeman, J.C.; Nayar, P.G.; Begley, T.P.; Villafranca, J.J. Stoichiometry and spectroscopic identity of copper centers in phenoxazinone synthase—A new addition to the blue copper oxidase family. *Biochemistry* **1993**, *32*, 4826–4830. [[CrossRef](#)]
29. Barry, C.E.; Nayar, P.G.; Begley, T.P. Phenoxazinone synthase-mechanism for the formation of the phenoxazinone chromophore of actinomycin. *Biochemistry* **1989**, *28*, 6323–6333. [[CrossRef](#)]
30. Hollstein, U. Actinomycin-chemistry and mechanism of action. *Chem. Rev.* **1974**, *74*, 625–652. [[CrossRef](#)]
31. Le Roes-Hill, M.; Goodwin, C.; Burton, S. Phenoxazinone synthase: What's in a name? *Trends Biotechnol.* **2009**, *27*, 248–258. [[CrossRef](#)]
32. Smith, A.W.; Camara-Artigas, A.; Wang, M.T.; Allen, J.P.; Francisco, W.A. Structure of phenoxazinone synthase from *Streptomyces antibioticus* reveals a new type 2 copper center. *Biochemistry* **2006**, *45*, 4378–4387. [[CrossRef](#)]
33. Sagar, S.; Sengupta, S.; Mota, A.J.; Chattopadhyay, S.K.; Ferao, A.E.; Riviere, E.; Lewis, W.; Naskar, S. Cubane-like tetranuclear Cu(II) complexes bearing a Cu₄O₄ core: Crystal structure, magnetic properties, DFT calculations and phenoxazinone synthase like activity. *Dalton Trans.* **2017**, *46*, 1249–1259. [[CrossRef](#)]
34. Mukherjee, C.; Weyhermuller, T.; Bothe, E.; Rentschier, E.; Chaudhuri, P. A Tetracopper(II)-Tetraradical cuboidal core and its reactivity as a functional model of phenoxazinone synthase. *Inorg. Chem.* **2007**, *46*, 9895–9905. [[CrossRef](#)]
35. Podder, N.; Mandal, S. Aerobic oxidation of 2-aminophenol catalysed by a series of mononuclear copper(II) complexes: Phenoxazinone synthase-like activity and mechanistic study. *New J. Chem.* **2020**, *44*, 12793–12805. [[CrossRef](#)]
36. Dhara, A.K.; Singh, U.P.; Ghosh, K. Radical pathways and O₂ participation in benzyl alcohol oxidation, and catechol and o-amino-phenol oxidase activity studies with novel zinc complexes: An experimental and theoretical investigation. *Inorg. Chem. Front.* **2016**, *3*, 1543–1558. [[CrossRef](#)]
37. Kaizer, J.; Csonka, R.; Speier, G. TEMPO-initiated oxidation of 2-aminophenol to 2-aminophenoxazin-3-one. *J. Mol. Catal. A* **2002**, *180*, 91–96. [[CrossRef](#)]
38. Khairy, M.; Mahmoud, A.H.; Khalil, K.M.S. Synthesis of highly crystalline LaFeO₃ nanospheres for phenoxazinone synthase mimicking activity. *RSC Adv.* **2021**, *11*, 17746–17754. [[CrossRef](#)]
39. Johnson, E.R.; Keinan, S.; Mori-Sanchez, P.; Contreras-Garcia, J.; Cohen, A.J.; Yang, W.T. Revealing Noncovalent Interactions. *J. Am. Chem. Soc.* **2010**, *132*, 6498–6506. [[CrossRef](#)]
40. Emamian, S.; Lu, T.; Kruse, H.; Emamian, H. Exploring Nature and Predicting Strength of Hydrogen Bonds: A Correlation Analysis Between Atoms-in-Molecules Descriptors, Binding Energies, and Energy Components of Symmetry-Adapted Perturbation Theory. *J. Comput. Chem.* **2019**, *40*, 2868–2881. [[CrossRef](#)]
41. Nanayakkara, S.; Tao, Y.W.; Kraka, E. Comment on “Exploring nature and predicting strength of hydrogen bonds: A correlation analysis between atoms-in-molecules descriptors, binding energies, and energy components of symmetry-adapted perturbation theory”. *J. Comput. Chem.* **2021**, *42*, 516–521. [[CrossRef](#)] [[PubMed](#)]
42. Rezac, J.; Hobza, P. Benchmark Calculations of Interaction Energies in Noncovalent Complexes and Their Applications. *Chem. Rev.* **2016**, *116*, 5038–5071. [[CrossRef](#)] [[PubMed](#)]
43. Hassanein, M.; Abdo, M.; Gerges, S.; El-Khalafy, S. Study of the oxidation of 2-aminophenol by molecular oxygen catalyzed by cobalt(II) phthalocyaninetetrasodiumsulfonate in water. *J. Mol. Catal. A* **2008**, *287*, 53–56. [[CrossRef](#)]
44. Simandi, L.I.; Barna, T.; Nemeth, S. Kinetics and mechanism of the cobaloxime(II)-catalysed oxidation of 2-aminophenol by dioxygen. A phenoxazinone synthase model involving free-radical intermediates. *J. Chem. Soc. Dalton Trans.* **1996**, *4*, 473–478. [[CrossRef](#)]
45. Szigyarto, I.C.; Simandi, T.M.; Simandi, L.I.; Korecz, L.; Nagy, N. A functional phenoxazinone synthase model based on dioximatomanganese(II)-Kinetics and mechanism of the catalytic oxidation of 2-aminophenols by dioxygen. *J. Mol. Catal. A* **2006**, *251*, 270–276. [[CrossRef](#)]
46. Chai, J.D.; Head-Gordon, M. Systematic optimization of long-range corrected hybrid density functionals. *J. Chem. Phys.* **2008**, *128*, 084106. [[CrossRef](#)]
47. Najibi, A.; Goerigk, L. DFT-D4 counterparts of leading meta-generalized-gradient approximation and hybrid density functionals for energetics and geometries. *J. Comput. Chem.* **2020**, *41*, 2562–2572. [[CrossRef](#)]
48. Grimme, S. Semiempirical hybrid density functional with perturbative second-order correlation. *J. Chem. Phys.* **2006**, *124*, 034108. [[CrossRef](#)]
49. Groom, C.R.; Bruno, I.J.; Lightfoot, M.P.; Ward, S.C. The Cambridge Structural Database. *Acta Crystallogr. Sect. B Struct. Sci. Cryst. Eng. Mat.* **2016**, *72*, 171–179. [[CrossRef](#)]
50. Suzuki, T.; Oshita, H.; Yajima, T.; Tani, F.; Abe, H.; Shimazaki, Y. Formation of the Cu^{II}-Phenoxy Radical by Reaction of O₂ with a Cu^{II}-Phenolate Complex via the Cu^I-Phenoxy Radical. *Chem. Eur. J.* **2019**, *25*, 15805–15814. [[CrossRef](#)]
51. Liu, J.Q.; Lorraine, S.C.; Dolinar, B.S.; Hoover, J.M. Aerobic Oxidation Reactivity of Well-Defined Cobalt(II) and Cobalt(III) Aminophenol Complexes. *Inorg. Chem.* **2022**, *61*, 6008–6016. [[CrossRef](#)]

52. Hoover, J.M.; Ryland, B.L.; Stahl, S.S. Mechanism of Copper(I)/TEMPO-Catalyzed Aerobic Alcohol Oxidation. *J. Am. Chem. Soc.* **2013**, *135*, 2357–2367. [CrossRef]
53. Gozzo, F. Radical and non-radical chemistry of the Fenton-like systems in the presence of organic substrates. *J. Mol. Catal. A* **2001**, *171*, 1–22. [CrossRef]
54. Sankaralingam, M.; Lee, Y.M.; Nam, W.; Fukuzumi, S. Amphoteric reactivity of metal-oxygen complexes in oxidation reactions. *Coord. Chem. Rev.* **2018**, *365*, 41–59. [CrossRef]
55. Zhao, Y.; Truhlar, D.G. The M06 suite of density functionals for main group thermochemistry, thermochemical kinetics, noncovalent interactions, excited states, and transition elements: Two new functionals and systematic testing of four M06-class functionals and 12 other functionals. *Theor. Chem. Acc.* **2008**, *120*, 215–241. [CrossRef]
56. Tao, J.M.; Perdew, J.P.; Staroverov, V.N.; Scuseria, G.E. Climbing the density functional ladder: Nonempirical meta-generalized gradient approximation designed for molecules and solids. *Phys. Rev. Lett.* **2003**, *91*, 146401. [CrossRef]
57. Staroverov, V.N.; Scuseria, G.E.; Tao, J.M.; Perdew, J.P. Comparative assessment of a new nonempirical density functional: Molecules and hydrogen-bonded complexes. *J. Chem. Phys.* **2003**, *119*, 12129–12137. [CrossRef]
58. Perdew, J.P.; Tao, J.M.; Staroverov, V.N.; Scuseria, G.E. Meta-generalized gradient approximation: Explanation of a realistic nonempirical density functional. *J. Chem. Phys.* **2004**, *120*, 6898–6911. [CrossRef]
59. Stephens, P.J.; Devlin, F.J.; Chabalowski, C.F.; Frisch, M.J. Ab-initio calculation of vibrational absorption and circular-dichroism spectra using density-functional force-fields. *J. Phys. Chem.* **1994**, *98*, 11623–11627. [CrossRef]
60. Adamo, C.; Barone, V. Toward reliable density functional methods without adjustable parameters: The PBE0 model. *J. Chem. Phys.* **1999**, *110*, 6158–6170. [CrossRef]
61. Ernzerhof, M.; Scuseria, G.E. Assessment of the Perdew-Burke-Ernzerhof exchange-correlation functional. *J. Chem. Phys.* **1999**, *110*, 5029–5036. [CrossRef]
62. Zhao, Y.; Truhlar, D.G. A new local density functional for main-group thermochemistry, transition metal bonding, thermochemical kinetics, and noncovalent interactions. *J. Chem. Phys.* **2006**, *125*, 194101. [CrossRef] [PubMed]
63. Perdew, J.P.; Burke, K.; Ernzerhof, M. Generalized gradient approximation made simple. *Phys. Rev. Lett.* **1996**, *77*, 3865–3868. [CrossRef] [PubMed]
64. Becke, A.D. Density-functional exchange-energy approximation with correct asymptotic-behavior. *Phys. Rev. A* **1988**, *38*, 3098–3100. [CrossRef] [PubMed]
65. Perdew, J.P. Density-functional approximation for the correlation-energy of the inhomogeneous electron-gas. *Phys. Rev. B* **1986**, *33*, 8822–8824. [CrossRef]
66. Brandenburg, J.G.; Bannwarth, C.; Hansen, A.; Grimme, S. B97-3c: A revised low-cost variant of the B97-D density functional method. *J. Chem. Phys.* **2018**, *148*, 13. [CrossRef]
67. Cohen, A.J.; Mori-Sanchez, P.; Yang, W.T. Challenges for Density Functional Theory. *Chem. Rev.* **2012**, *112*, 289–320. [CrossRef]
68. Bursch, M.; Mewes, J.M.; Hansen, A.; Grimme, S. Best-Practice DFT Protocols for Basic Molecular Computational Chemistry. *Angew. Chem. Int. Ed.* **2022**, *61*, e202205735. [CrossRef]
69. Wolters, L.P.; Schyman, P.; Pavan, M.J.; Jorgensen, W.L.; Bickelhaupt, F.M.; Kozuch, S. The many faces of halogen bonding: A review of theoretical models and methods. *Wiley Interdiscip. Rev. Comput. Mol. Sci.* **2014**, *4*, 523–540. [CrossRef]
70. Kozuch, S.; Martin, J.M.L. Halogen Bonds: Benchmarks and Theoretical Analysis. *J. Chem. Theor. Comput.* **2013**, *9*, 1918–1931. [CrossRef]
71. Simon, L.; Goodman, J.M. How reliable are DFT transition structures? Comparison of GGA, hybrid-meta-GGA and meta-GGA functionals. *Org. Biomol. Chem.* **2011**, *9*, 689–700. [CrossRef]
72. Murakami, M.; Ishida, N. Beta-Scission of Alkoxy Radicals in Synthetic Transformations. *Chem. Lett.* **2017**, *46*, 1692–1700. [CrossRef]
73. Tran, B.L.; Li, B.J.; Driess, M.; Hartwig, J.F. Copper-Catalyzed Intermolecular Amidation and Imidation of Unactivated Alkanes. *J. Am. Chem. Soc.* **2014**, *136*, 2555–2563. [CrossRef]
74. Nesterova, O.V.; Kopylovich, M.N.; Nesterov, D.S. A Comparative Study of the Catalytic Behaviour of Alkoxy-1,3,5-Triazapentadiene Copper(II) Complexes in Cyclohexane Oxidation. *Inorganics* **2019**, *7*, 82. [CrossRef]
75. Gryca, I.; Czerwinska, K.; Machura, B.; Chrobok, A.; Shul'pina, L.S.; Kuznetsov, M.L.; Nesterov, D.S.; Kozlov, Y.N.; Pombeiro, A.J.L.; Varyan, I.A.; et al. High Catalytic Activity of Vanadium Complexes in Alkane Oxidations with Hydrogen Peroxide: An Effect of 8-Hydroxyquinoline Derivatives as Noninnocent Ligands. *Inorg. Chem.* **2018**, *57*, 1824–1839. [CrossRef]
76. Astakhov, G.S.; Bilyachenko, A.N.; Korlyukov, A.A.; Levitsky, M.M.; Shul'pina, L.S.; Bantreil, X.; Lamaty, F.; Vologzhanina, A.V.; Shubina, E.S.; Dorovatovskii, P.V.; et al. High-Cluster Cu₉ Cage Silsesquioxanes: Synthesis, Structure, and Catalytic Activity. *Inorg. Chem.* **2018**, *57*, 11524–11529. [CrossRef]
77. Shul'pin, G.B.; Nesterov, D.S.; Shul'pina, L.S.; Pombeiro, A.J.L. A hydroperoxo-rebound mechanism of alkane oxidation with hydrogen peroxide catalyzed by binuclear manganese(IV) complex in the presence of an acid with involvement of atmospheric dioxygen. *Inorg. Chim. Acta* **2017**, *455*, 666–676. [CrossRef]
78. Nesterova, O.V.; Nesterov, D.S.; Krogul-Sobczak, A.; Guedes da Silva, M.F.C.; Pombeiro, A.J.L. Synthesis, crystal structures and catalytic activity of Cu(II) and Mn(III) Schiff base complexes: Influence of additives on the oxidation catalysis of cyclohexane and 1-phenylethanol. *J. Mol. Catal. A* **2017**, *426*, 506–515. [CrossRef]

79. Wierzchowski, P.T.; Zatorski, L.W. Determination of cycle C-6 and C-7 peroxides and hydroperoxides by gas chromatography. *Chromatographia* **2000**, *51*, 83–86. [[CrossRef](#)]
80. Vinogradov, M.M.; Kozlov, Y.N.; Bilyachenko, A.N.; Nesterov, D.S.; Shul'pina, L.S.; Zubavichus, Y.V.; Pombeiro, A.J.L.; Levitsky, M.M.; Yalymov, A.I.; Shul'pin, G.B. Alkane oxidation with peroxides catalyzed by cage-like copper(II) silsesquioxanes. *New J. Chem.* **2015**, *39*, 187–199. [[CrossRef](#)]
81. Kim, H.Y.; Oh, K. Recent advances in the copper-catalyzed aerobic C_{sp3}-H oxidation strategy. *Org. Biomol. Chem.* **2021**, *19*, 3569–3583. [[CrossRef](#)] [[PubMed](#)]
82. Thapa, S.; Shrestha, B.; Gurung, S.K.; Giri, R. Copper-catalysed cross-coupling: An untapped potential. *Org. Biomol. Chem.* **2015**, *13*, 4816–4827. [[CrossRef](#)] [[PubMed](#)]
83. McCann, S.D.; Stahl, S.S. Copper-Catalyzed Aerobic Oxidations of Organic Molecules: Pathways for Two-Electron Oxidation with a Four-Electron Oxidant and a One-Electron Redox-Active Catalyst. *Acc. Chem. Res.* **2015**, *48*, 1756–1766. [[CrossRef](#)] [[PubMed](#)]
84. Allen, S.E.; Walvoord, R.R.; Padilla-Salinas, R.; Kozlowski, M.C. Aerobic Copper-Catalyzed Organic Reactions. *Chem. Rev.* **2013**, *113*, 6234–6458. [[CrossRef](#)] [[PubMed](#)]
85. Shiri, P.; Aboonajmi, J. A systematic review on silica-, carbon-, and magnetic materials-supported copper species as efficient heterogeneous nanocatalysts in “click” reactions. *Beilst. J. Org. Chem.* **2020**, *16*, 551–586. [[CrossRef](#)]
86. Bruker. *APEX2 & SAINT*; AXS Inc.: Madison, WI, USA, 2004.
87. Sheldrick, G.M. Crystal structure refinement with SHELXL. *Acta Crystallogr. C Struct. Chem.* **2015**, *71*, 3–8. [[CrossRef](#)]
88. Dolomanov, O.V.; Bourhis, L.J.; Gildea, R.J.; Howard, J.A.K.; Puschmann, H. OLEX2: A complete structure solution, refinement and analysis program. *J. Appl. Crystallogr.* **2009**, *42*, 339–341. [[CrossRef](#)]
89. Shul'pin, G.B. Metal-catalyzed hydrocarbon oxygenations in solutions: The dramatic role of additives: A review. *J. Mol. Catal. A* **2002**, *189*, 39–66. [[CrossRef](#)]
90. Neese, F.; Wennmohs, F.; Becker, U.; Riplinger, C. The ORCA quantum chemistry program package. *J. Chem. Phys.* **2020**, *152*, 18. [[CrossRef](#)]
91. Neese, F. Software update: The ORCA program system, version 4.0. *Wiley Interdiscipl. Rev. Comput. Mol. Sci.* **2018**, *8*, e1327. [[CrossRef](#)]
92. Neese, F. The ORCA program system. *Wiley Interdiscipl. Rev. Comput. Mol. Sci.* **2012**, *2*, 73–78. [[CrossRef](#)]
93. Hertwig, R.H.; Koch, W. On the parameterization of the local correlation functional. What is Becke-3-LYP? *Chem. Phys. Lett.* **1997**, *268*, 345–351. [[CrossRef](#)]
94. Zheng, J.J.; Xu, X.F.; Truhlar, D.G. Minimally augmented Karlsruhe basis sets. *Theor. Chem. Acc.* **2011**, *128*, 295–305. [[CrossRef](#)]
95. Caldeweyher, E.; Bannwarth, C.; Grimme, S. Extension of the D3 dispersion coefficient model. *J. Chem. Phys.* **2017**, *147*, 034112. [[CrossRef](#)]
96. Riplinger, C.; Sandhoefer, B.; Hansen, A.; Neese, F. Natural triple excitations in local coupled cluster calculations with pair natural orbitals. *J. Chem. Phys.* **2013**, *139*, 134101. [[CrossRef](#)]
97. Stoychev, G.L.; Auer, A.A.; Neese, F. Automatic Generation of Auxiliary Basis Sets. *J. Chem. Theor. Comput.* **2017**, *13*, 554–562. [[CrossRef](#)]
98. Asgeirsson, V.; Birgisson, B.O.; Bjornsson, R.; Becker, U.; Neese, F.; Riplinger, C.; Jonsson, H. Nudged Elastic Band Method for Molecular Reactions Using Energy-Weighted Springs Combined with Eigenvector Following. *J. Chem. Theor. Comput.* **2021**, *17*, 4929–4945. [[CrossRef](#)]
99. Harvey, J.N.; Aschi, M.; Schwarz, H.; Koch, W. The singlet and triplet states of phenyl cation. A hybrid approach for locating minimum energy crossing points between non-interacting potential energy surfaces. *Theor. Chem. Acc.* **1998**, *99*, 95–99. [[CrossRef](#)]
100. Barone, V.; Cossi, M. Quantum calculation of molecular energies and energy gradients in solution by a conductor solvent model. *J. Phys. Chem. A* **1998**, *102*, 1995–2001. [[CrossRef](#)]
101. Marenich, A.V.; Cramer, C.J.; Truhlar, D.G. Universal Solvation Model Based on Solute Electron Density and on a Continuum Model of the Solvent Defined by the Bulk Dielectric Constant and Atomic Surface Tensions. *J. Phys. Chem. B* **2009**, *113*, 6378–6396. [[CrossRef](#)]
102. Hirata, S.; Head-Gordon, M. Time-dependent density functional theory within the Tamm-Dancoff approximation. *Chem. Phys. Lett.* **1999**, *314*, 291–299. [[CrossRef](#)]
103. Shao, Y.H.; Mei, Y.; Sundholm, D.; Kaila, V.R.I. Benchmarking the Performance of Time-Dependent Density Functional Theory Methods on Biochromophores. *J. Chem. Theor. Comput.* **2020**, *16*, 587–600. [[CrossRef](#)] [[PubMed](#)]
104. Nesterova, O.V.; Vassilyeva, O.Y.; Skelton, B.W.; Benko, A.; Pombeiro, A.J.L.; Nesterov, D.S. A novel *o*-vanillin Fe(III) complex catalytically active in C-H oxidation: Exploring the magnetic exchange interactions and spectroscopic properties with different DFT functionals. *Dalton Trans.* **2021**, *50*, 14782–14796. [[CrossRef](#)] [[PubMed](#)]
105. Hanwell, M.D.; Curtis, D.E.; Lonie, D.C.; Vandermeersch, T.; Zurek, E.; Hutchison, G.R. Avogadro: An advanced semantic chemical editor, visualization, and analysis platform. *J. Cheminform.* **2012**, *4*, 17. [[CrossRef](#)]
106. Lu, T.; Chen, F.W. Multiwfn: A multifunctional wavefunction analyzer. *J. Comput. Chem.* **2012**, *33*, 580–592. [[CrossRef](#)]